The triggering of starbursts in low-mass galaxies

Lelli, Federico; Verheijen, Marc; Fraternali, Filippo

Published in:
Monthly Notices of the Royal Astronomical Society

DOI:
10.1093/mnras/stu1804

Publication date:
2014

Monthly Notices of the ROYAL ASTRONOMICAL SOCIETY
MNRAS **445,** 1694–1712 (2014) doi:10.1093/mnras/stu1804

The triggering of starbursts in low-mass galaxies

Federico Lelli,[1,2]★ Marc Verheijen[2] and Filippo Fraternali[1,3]

[1]*Department of Astronomy, Case Western Reserve University, 10900 Euclid Ave, Cleveland, OH 44106, USA*
[2]*Kapteyn Astronomical Institute, University of Groningen, Postbus 800, NL-9700 AV Groningen, the Netherlands*
[3]*Department of Physics and Astronomy, University of Bologna, via Berti Pichat 6/2, I-40127 Bologna, Italy*

Accepted 2014 September 2. Received 2014 August 7; in original form 2014 April 10

ABSTRACT

Strong bursts of star formation in galaxies may be triggered either by internal or external mechanisms. We study the distribution and kinematics of the H I gas in the outer regions of 18 nearby starburst dwarf galaxies that have accurate star formation histories from *Hubble Space Telescope* observations of resolved stellar populations. We find that starburst dwarfs show a variety of H I morphologies, ranging from heavily disturbed H I distributions with major asymmetries, long filaments, and/or H I–stellar offsets to lopsided H I distributions with minor asymmetries. We quantify the outer H I asymmetry for both our sample and a control sample of typical dwarf irregulars. Starburst dwarfs have more asymmetric outer H I morphologies than typical irregulars, suggesting that some external mechanism triggered the starburst. Moreover, galaxies hosting an old burst ($\gtrsim$100 Myr) have more symmetric H I morphologies than galaxies hosting a young one ($\lesssim$100 Myr), indicating that the former ones probably had enough time to regularize their outer H I distribution since the onset of the burst. We also investigate the nearby environment of these starburst dwarfs and find that most of them (∼80 per cent) have at least one potential perturber at a projected distance $\lesssim$200 kpc. Our results suggest that the starburst is triggered either by past interactions/mergers between gas-rich dwarfs or by direct gas infall from the intergalactic medium.

Key words: galaxies: dwarf – galaxies: evolution – galaxies: interactions – galaxies: irregular – galaxies: kinematics and dynamics – galaxies: starburst.

1 INTRODUCTION

The mechanisms that trigger strong bursts of star formation in low-mass galaxies are poorly understood. Unlike spiral galaxies, gas-rich dwarfs usually do not have density waves and stellar bars, thus internal mechanisms such as bar-driven gas inflows are generally ruled out (e.g. Hunter & Elmegreen 2004). Other internal mechanisms have been proposed, like torques due to massive star-forming clumps (Elmegreen, Zhang & Hunter 2012), triaxial dark matter haloes (Bekki & Freeman 2002), or bars made of dark matter (Hunter & Elmegreen 2004). External mechanisms are also possible, like tidal perturbations from nearby companions (e.g. Noguchi 1988), interactions/mergers between gas-rich dwarfs (e.g. Bekki 2008), or cold gas accretion from the intergalactic medium (IGM; e.g. Silk, Wyse & Shields 1987). In particular, cosmological models predict that low-mass galaxies should accrete most of their gas through cold flows, reaching the central parts of the dark matter halo without being shock heated to the virial temperature (e.g. Dekel & Birnboim 2006). This process may still take place at $z \simeq 0$ in low-density environments (Kereš et al. 2005), thus isolated starburst dwarfs in the nearby Universe are prime locations to search for cold gas accretion.

In the literature, starburst dwarfs are referred to with several names, often related to the observational technique used to identify the starburst. Common names are (i) blue compact dwarfs (BCDs) as they have blue colours and high surface brightnesses (e.g. Gil de Paz, Madore & Pevunova 2003); (ii) H II galaxies as they have integrated spectra with strong emission lines (e.g. Terlevich et al. 1991; Taylor et al. 1995); and (iii) amorphous dwarfs as they may have peculiar morphologies dominated by a few giant star-forming regions (e.g. Gallagher & Hunter 1987; Marlowe, Meurer & Heckman 1999). Hereafter we use the general term 'starburst dwarfs' to indicate any low-mass galaxy experiencing an enhanced period of star formation activity.

In Lelli, Verheijen & Fraternali (2014b, hereafter LVF14), we studied the H I content of 18 starburst dwarfs and found that disturbed H I kinematics are more common in starburst dwarfs (∼50 per cent) than in typical star-forming irregulars (Irrs; ∼10 per cent). This may be related to the starburst trigger (interactions/mergers or disc instabilities), but may also be a consequence of feedback from supernovae and stellar winds, making it difficult to distinguish between different triggering mechanisms. About 50 per cent of our starburst dwarfs, instead, have a regularly

★ E-mail: federico.lelli@case.edu

Table 1. Galaxy sample.

Name	Alternative name	RA (J2000)	Dec. (J2000)	V_{sys} (km s^{-1})	V_{rot} (km s^{-1})	Dist (Mpc)	M_R (mag)	R_{opt} (kpc)	12 + log(O/H)	Ref.
NGC 625	ESO 297−G005	01 35 04.3	−41 26 15	398 ± 6	30 ± 5	3.9 ± 0.4	−17.25 ± 0.24	3.3	8.08 ± 0.12	a, g, l
NGC 1569	UGC 3056	04 30 49.0	+64 50 53	−80 ± 10	50 ± 5	3.4 ± 0.2	−17.14 ± 0.25	3.0	8.19 ± 0.02	a, h, m
NGC 1705	ESO 158−G013	04 54 13.9	−53 21 25	635 ± 2	72 ± 10	5.1 ± 0.6	−16.35 ± 0.26	1.5	8.21 ± 0.05	b, i, l
NGC 2366	UGC 3851	07 28 51.9	+69 12 34	103 ± 1	49 ± 6	3.2 ± 0.4	−16.64 ± 0.27	4.4	7.91 ± 0.05	a, h, l
NGC 4068	UGC 7047	12 04 02.7	+52 35 28	206 ± 2	39 ± 5	4.3 ± 0.1	−15.67 ± 0.05	1.8	...	a, h
NGC 4163	UGC 7199	12 12 09.0	+36 10 11	158 ± 4	10 ± 5	3.0 ± 0.1	−14.81 ± 0.10	1.0	7.56 ± 0.14	a, h, l
NGC 4214	UGC 7278	12 15 38.8	+36 19 39	291 ± 1	81 ± 9	2.7 ± 0.2	−17.77 ± 0.24	2.2	8.22 ± 0.05	a, h, l
NGC 4449	UGC 7592	12 28 10.8	+44 05 37	210 ± 5	35 ± 5	4.2 ± 0.5	−18.88 ± 0.26	3.3	8.26 ± 0.09	a, h, l
NGC 5253	Haro 10	13 39 56.0	−31 38 31	410 ± 10	...	3.5 ± 0.4	−17.61 ± 0.27	2.1	8.12 ± 0.05	a, g, k
NGC 6789	UGC 11425	19 16 41.9	+63 58 17	−151 ± 2	57 ± 9	3.6 ± 0.2	−15.09 ± 0.14	0.7	...	a, i
UGC 4483	...	08 37 03.4	+69 46 31	158 ± 2	19 ± 2	3.2 ± 0.2	−12.97 ± 0.19	0.6	7.56 ± 0.03	a, i, l
UGC 6456	VII Zw 403	11 27 57.2	+78 59 48	−102 ± 4	10 ± 5	4.3 ± 0.1	−14.41 ± 0.05	1.2	7.69 ± 0.01	a, j, n
UGC 6541	Mrk 178	11 33 28.9	+49 14 22	250 ± 2	...	4.2 ± 0.2	−14.61 ± 0.10	0.9	7.82 ± 0.06	c, j, l
UGC 9128	DDO 187	14 15 56.8	+23 03 22	150 ± 3	24 ± 4	2.2 ± 0.1	−12.82 ± 0.12	0.6	7.75 ± 0.05	a, h, l
UGCA 290	Arp 211	12 37 22.1	+38 44 41	468 ± 5	...	6.7 ± 0.4	−14.09 ± 0.18	0.9	...	d, i
I Zw 18	Mrk 116	09 34 02.0	+55 14 25	767 ± 4	38 ± 4	18.2 ± 1.4	−14.99 ± 0.26	0.5	7.20 ± 0.01	e, j, k
I Zw 36	Mrk 209	12 26 16.8	+48 29 39	277 ± 2	29 ± 2	5.8 ± 0.5	−14.88 ± 0.23	0.9	7.77 ± 0.01	f, i, k
SBS 1415+437	...	14 17 02.1	+43 30 19	616 ± 2	18 ± 2	13.6 ± 1.4	−15.90 ± 0.25	2.4	7.62 ± 0.03	a, i, o

Notes. The galaxy centre is derived from *R*- or *V*-band images, while the rotation velocity V_{rot} is measured at the outermost radius accessible by H I data at relatively high spatial resolutions (LVF14). Distances are derived from the tip of the red giant branch (TRGB). The optical radius R_{opt} is defined as 3.2 exponential scalelengths. The last column provides references for the distance, the integrated photometry, and the ionized gas metallicity, respectively.
References: a – McQuinn et al. (2010); b – Annibali et al. (2003); c – Schulte-Ladbeck et al. (2000); d – Crone et al. (2002); e – Annibali et al. (2013); f – Schulte-Ladbeck et al. (2001); g – Lauberts & Valentijn (1989); h – Swaters & Balcells (2002); i – Gil de Paz et al. (2003); j – Papaderos et al. (2002); k – Izotov & Thuan (1999); l – Berg et al. (2012); m – Kobulnicky & Skillman (1997); n – Thuan & Izotov (2005); o – Guseva et al. (2003).

rotating H I disc that allows us to derive rotation curves and investigate the internal mass distribution. In Lelli, Fraternali & Verheijen (2014a), we found that the inner rotation curves of starburst dwarfs rise more steeply than those of typical Irrs (see also van Zee, Salzer & Skillman 2001; Lelli et al. 2012a,b), suggesting that there is a close link between the intense star formation activity and the shape of the gravitational potential. A central concentration of mass (gas, stars, and dark matter) seems to be a characterizing property of starburst dwarfs and must be tightly linked to the mechanism (either internal or external) that triggers the starburst (see Lelli et al. 2014a, for an in-depth discussion).

Environmental studies also provide important clues about the triggering mechanism. In general, star-forming dwarfs tend to populate low-density environments (e.g. Iovino, Melnick & Shaver 1988; Salzer 1989; Lee et al. 2000; Telles & Maddox 2000) and are not necessarily associated with *bright* galaxies (e.g. Campos-Aguilar & Moles 1991; Campos-Aguilar, Moles & Masegosa 1993; Pustilnik et al. 1995; Telles & Terlevich 1995), suggesting that tidal interactions with *massive* companions are *not* the dominant starburst trigger. The possibility of interactions with low-luminosity, low-surface-brightness (LSB) galaxies, however, remains open (e.g. Méndez, Esteban & Balcells 1999; Méndez & Esteban 2000; Noeske et al. 2001; Pustilnik et al. 2001b), given that these objects are usually under-represented in optical catalogues. Moreover, if the starburst is due to a *past* interaction/merger with a LSB dwarf, the resulting tidal features would have very low surface brightnesses and be difficult to unambiguously identify, unless deep optical imaging is available (e.g. López-Sánchez 2010; Martínez-Delgado et al. 2012).

Alternatively, deep 21-cm-line observations can be used to search for gas-rich companions, infalling gas, or signatures of past interactions/mergers (e.g. Sancisi et al. 2008). Taylor, Brinks & Skillman (1993) and Taylor et al. (1995, 1996) obtained low-resolution Very Large Array (VLA) observations of 21 starburst dwarfs and 17 LSB dwarfs, and concluded that starburst dwarfs have nearby 'H I companions' more than twice as often as LSB dwarfs. However, given the poor angular resolution of these observations, in most cases it was not possible to distinguish between actual H I companions and asymmetries in the outer H I distribution. Detailed studies of the H I gas in the outer regions of starburst dwarfs have been so far restricted to individual objects or small galaxy samples. These works have revealed that several starburst dwarfs show extended and filamentary H I structures, which may indicate either a recent interaction/merger or cold gas accretion from the environment, e.g. NGC 1569 (Stil & Israel 2002), IC 10 (Manthey & Oosterloo 2008), and NGC 5253 (López-Sánchez et al. 2012). In some cases, the presence of a nearby companion and/or of stellar tidal features clearly points to an interaction/merger between gas-rich dwarfs, e.g. II Zw 40 (van Zee, Skillman & Salzer 1998), II Zw 70/71 (Cox et al. 2001), and I Zw 18 (Lelli et al. 2012a). However, some starburst dwarfs seem to have relatively symmetric and unperturbed H I discs, e.g. NGC 2915 (Elson, de Blok & Kraan-Korteweg 2011) and VII Zw 403 (Simpson et al. 2011). The relative fraction of starburst dwarfs with symmetric/asymmetric H I morphologies in their outer regions is unclear, as well as the relation between the extended H I emission and the starburst activity.

In this paper we investigate the hypothesis that starbursts in dwarf galaxies are triggered by external mechanisms. To this aim, we study in detail the H I emission in the outer regions of 18 starburst dwarfs. The properties of our galaxy sample have been described in LVF14 and are summarized in Tables 1 and 2. In short, we selected galaxies that satisfy two criteria: (i) they have been resolved into single stars by *Hubble Space Telescope* (*HST*) observations, providing star formation rates (SFRs) and detailed star formation histories (SFHs) from the modelling of colour–magnitude diagrams (CMDs; e.g. McQuinn et al. 2010); and (ii) they have a birth rate parameter $b = \mathrm{SFR}/\overline{\mathrm{SFR}} \gtrsim 3$, identifying a starburst (Kennicutt 1998). As far as we are aware of, 25 dwarf galaxies observed with the *HST*

Table 2. Properties of the starburst.

Galaxy	b	SFR_0	SFR_p	$\Sigma_{SFR}(0)$	$\Sigma_{SFR}(t_p)$	$\log(sSFR_0)$	$\log(sSFR_p)$	t_p	Ref.
		$(10^{-3}\,M_\odot\,yr^{-1})$		$(10^{-3}\,M_\odot\,yr^{-1}\,kpc^{-2})$		(Gyr^{-1})		(Myr)	
NGC 625	3.0 ± 0.1	4 ± 2	86 ± 20	0.12 ± 0.06	2.5 ± 0.6	−2.66 ± 0.63	−1.33 ± 0.45	820 ± 180	a
NGC 1569	21 ± 1	80 ± 15	240 ± 10	2.8 ± 0.5	8.5 ± 0.3	−1.79 ± 0.21	−1.31 ± 0.11	40 ± 10	a
NGC 1705	∼6	314 ± 78	314 ± 78	44 ± 11	44 ± 11	−0.65 ± 0.56	−0.65 ± 0.56	3.0 ± 1.5	b
NGC 2366	5.6 ± 0.4	43 ± 9	160 ± 10	0.7 ± 0.1	2.6 ± 0.2	−1.63 ± 0.24	−1.06 ± 0.13	450 ± 50	a
NGC 4068	4.7 ± 0.3	31 ± 7	42 ± 3	3.0 ± 0.7	4.5 ± 0.3	−1.70 ± 0.26	−1.56 ± 0.15	360 ± 40	a
NGC 4163	2.9 ± 0.6	5.2 ± 1.6	12 ± 3	1.6 ± 0.5	3.8 ± 0.9	−2.13 ± 0.43	−1.77 ± 0.39	450 ± 50	a
NGC 4214	3.1 ± 0.9	64 ± 13	130 ± 40	4.2 ± 0.8	8.5 ± 2.6	−1.49 ± 0.32	−1.18 ± 0.40	450 ± 50	a
NGC 4449	6.0 ± 0.5	970 ± 70	970 ± 70	28 ± 2	28 ± 2	−1.18 ± 0.18	−1.18 ± 0.18	5 ± 3	a
NGC 5253	9.0 ± 0.9	162 ± 13	400 ± 40	12 ± 0.9	29 ± 3	−1.82 ± 0.16	−1.43 ± 0.17	450 ± 50	a
NGC 6789	3.8 ± 1.3	3.0 ± 1.3	15 ± 5	1.9 ± 0.8	9.7 ± 3.2	−2.21 ± 0.52	−1.51 ± 0.44	565 ± 65	a
UGC 4483	14 ± 3	11 ± 4	11 ± 2	9.7 ± 1.8	8.8 ± 3.5	−0.80 ± 0.27	−0.84 ± 0.45	565 ± 65	a
UGC 6456	7.6 ± 1.1	23 ± 3	23 ± 3	5.1 ± 0.7	5.1 ± 0.7	−1.18 ± 0.42	−1.18 ± 0.42	16 ± 8	a
UGC 6541	∼3	3.0 ± 1.5	...	1.2 ± 0.6	...	−1.27 ± 0.71	...	...	c
UGC 9128	6.3 ± 1.4	0.7 ± 0.4	5 ± 1	0.6 ± 0.3	4.4 ± 0.9	−2.11 ± 0.59	−1.26 ± 0.25	150 ± 50	a
UGCA 290	∼3	11 ± 8	42 ± 15	4.3 ± 3.1	16 ± 6	−0.80 ± 0.88	−0.22 ± 0.61	15 ± 5	d
I Zw 18	∼30	100 ± 50	100 ± 50	127 ± 64	127 ± 64	−0.07 ± 0.73	−0.07 ± 0.73	10 ± 5	e
I Zw 36	∼7	25 ± 12	...	9.8 ± 4.7	...	−0.35 ± 0.69	...	...	f
SBS 1415+437	∼12	40 ± 7	150 ± 10	2.2 ± 0.4	8.3 ± 0.5	−1.47 ± 0.25	−0.90 ± 0.19	450 ± 50	a

Notes. For a detailed description of these quantities, we refer to Section 4.3. For UGC 6541 and I Zw 36, the recent SFH ($\lesssim$ 1 Gyr) is not well constrained due to the limited photometric depth of the CMDs, thus we have no robust estimate of $\Sigma_{SFR}(t_p)$, $sSFR_p$, and t_p. Another problematic case is I Zw 18, where we prefer to use the SFR derived from Hα observations rather than the value derived from fitting the CMD.
References: a – McQuinn et al. (2010); b – Annibali et al. (2003); c – Schulte-Ladbeck et al. (2000); d – Crone et al. (2002); e – Annibali et al. (2013); f – Schulte-Ladbeck et al. (2001).

satisfy these criteria; we collected new and archival H I data for 18 of them. Note that the birth rate parameter of a galaxy is generally very difficult to measure. According to Lee et al. (2009), galaxies with $b \gtrsim 2.5$–3 have Hα equivalent widths larger than ∼100 Å, and constitute only ∼6 per cent of the population of star-forming dwarfs at $z = 0$ (but see McQuinn et al. 2010 regarding the limitations of Hα observations to identify starburst dwarfs). Here we consider birth rate parameters derived directly from the SFHs as $SFR_p/\overline{SFR}$, where SFR_p is the peak SFR over the past 1 Gyr and $\overline{SFR}$ is the average SFR over the past 6 Gyr (see McQuinn et al. 2010). Thus, the *HST* information allows us to unambiguously identify starburst dwarfs, which generally constitute a small subset of star-forming dwarfs, and also to investigate possible relations between the H I emission in the outer galaxy regions and the detailed starburst properties (starburst time-scales, starburst intensity, etc.).

2 DATA ANALYSIS

For the 18 galaxies in our sample, we collected both new and archival 21-cm-line observations from the VLA, the Westerbork Synthesis Radio Telescope (WSRT), and the Australia Telescope Compact Array (ATCA). Archival observations were available for 15 galaxies, mostly from the following projects (see Table 3): the Westerbork HI survey of spiral and irregular galaxies (WHISP; Swaters et al. 2002), The HI Nearby Galaxy Survey (THINGS; Walter et al. 2008), Local Irregulars That Trace Luminosity Extremes (LITTLE)–THINGS (Hunter et al. 2012), and VLA-ACS Nearby Galaxy Survey Treasury (VLA-ANGST; Ott et al. 2012). New H I observations were obtained for the remaining three objects using the VLA and the WSRT. In LVF14, we described the reduction of these observations and presented H I data at relatively high spatial resolutions (ranging from 5 to 30 arcsec depending on the individual galaxy properties). Here we analyse H I data cubes at lower spatial resolutions, which are more sensitive to low column density gas in the outer regions (see Table 3). We use the same data set as in LVF14 except for two objects: NGC 4449 and UGC 4483. For NGC 4449, the H I data cube from THINGS (Walter et al. 2008) covers a relatively small region on the sky, thus here we use the total H I map and velocity field from Hunter et al. (1998), which were obtained from VLA D-array observations in a 3 × 3 pointing mosaic (covering ∼1°). For UGC 4483, in Lelli et al. (2012b) we reduced and analysed archival H I data obtained with the B- and C-arrays of the VLA, but here we use the data cube from Ott et al. (2012) that includes also new D-array observations, probing low column density gas on larger angular scales.

For every galaxy, we chose the optimal spatial resolution using the following approach. We first inspected the H I cube at the highest spatial and spectral resolutions available. Then, this cube was progressively smoothed in the image plane to 10, 20, 30, and 40 arcsec, and total H I maps at different spatial resolutions were constructed by summing masked channel maps. The smoothing procedure was halted when the total H I map reached a 3σ column density sensitivity of $\sim 10^{20}$ atoms cm^{-2}, which is adequate to investigate the H I morphology in the outer regions (e.g. Swaters et al. 2002) and, at the same time, allows us to preserve a relatively high angular resolution (typically 20 arcsec except for four cases, see Table 3). The masks were obtained by smoothing the cubes in velocity to ∼10 km s^{-1} and in the image plane to 1 arcmin (2 arcmin for NGC 2366, NGC 4214, and NGC 5253 given their large angular extent), and clipping at $3\sigma_s$ (σ_s is the rms noise in the smoothed cube). For NGC 4214, the cube was smoothed in velocity to only ∼2.6 km s^{-1} because only a few line-free channels were available at its high-velocity end. All the masks were visually inspected; residual noise peaks and Galactic emission were interactively blotted out. Note that the original, high-resolution cubes were obtained using a robust weighting technique (Briggs 1995) with robust parameter $\Re \simeq 0$, thus they have relatively low column density sensitivity but their beam profile is close to a Gaussian shape. We avoided using natural-weighted data cubes

Table 3. Properties of the H I data cubes.

Galaxy	Telescope	Source	Smoothed beam (arcsec^2)	Smoothed beam (pc^2)	Ch. sep. (km s^{-1})	Taper	Rms noise (mJy beam^{-1})	$N_{\rm H\,I}(3\sigma)$ (10^{20} cm^{-2})	$N_{\rm H\,I}(3\sigma)$ (M$_\odot$ pc^{-2})
NGC 625	VLA	a	30.0 × 30.0	567 × 567	2.6	Hann.	2.6	1.1 ± 0.5	0.9 ± 0.4
NGC 1569	VLA	b	20.0 × 20.0	330 × 330	2.6	Hann.	1.1	1.6 ± 0.7	1.3 ± 0.6
NGC 1705	ATCA	c	20.0 × 20.0	494 × 494	3.5	Hann.	1.2	1.1 ± 0.4	0.9 ± 0.3
NGC 2366	VLA	b	20.0 × 20.0	310 × 310	2.6	Hann.	1.3	1.5 ± 0.6	1.2 ± 0.5
NGC 4068	WSRT	d	30.0 × 30.0	625 × 625	2.0	Unif.	4.4	1.4 ± 0.5	1.2 ± 0.4
NGC 4163	VLA	b	20.0 × 20.0	290 × 290	1.3	Hann.	1.3	0.9 ± 0.3	0.8 ± 0.3
NGC 4214	VLA	b	30.0 × 30.0	393 × 393	1.3	Hann.	3.0	1.2 ± 0.6	1.0 ± 0.5
NGC 4449	VLA	e	62.0 × 54.0	1262 × 1099	5.2	Hann.	1.3	∼0.7	∼0.6
NGC 5253	ATCA	f	40.0 × 40.0	679 × 679	9.0	Unif.	2.7	1.0 ± 0.3	0.8 ± 0.3
NGC 6789	WSRT	a	20.0 × 20.0	349 × 349	2.0	Unif.	1.3	1.0 ± 0.3	0.8 ± 0.3
UGC 4483	VLA	g	20.0 × 20.0	310 × 310	2.6	Hann.	1.6	1.1 ± 0.3	0.9 ± 0.3
UGC 6456	VLA	a	20.0 × 20.0	417 × 417	2.6	Hann.	2.4	1.6 ± 0.7	1.3 ± 0.6
UGC 6541	VLA	b	20.0 × 20.0	408 × 408	1.3	Hann.	1.8	1.4 ± 0.4	1.2 ± 0.3
UGC 9128	VLA	b	20.0 × 20.0	213 × 213	2.6	Hann.	1.6	1.3 ± 0.4	1.0 ± 0.3
UGCA 290	VLA	a	20.0 × 20.0	650 × 650	1.6	Unif.	2.0	1.1 ± 0.3	0.9 ± 0.3
I Zw 18	VLA	h	20.0 × 20.0	1765 × 1765	1.3	Hann.	1.0	1.0 ± 0.6	0.8 ± 0.4
I Zw 36	VLA	b	20.0 × 20.0	572 × 572	2.6	Hann.	1.9	1.3 ± 0.4	1.0 ± 0.3
SBS 1415+437	VLA	a	20.0 × 20.0	1319 × 1319	1.6	Unif.	2.8	1.3 ± 0.3	1.0 ± 0.3

References: a – LVF14; b – Hunter et al. (2012); c – Elson, de Blok & Kraan-Korteweg (2013); d – Swaters et al. (2002); e – Hunter et al. (1998); f – López-Sánchez et al. (2012); g – Ott et al. (2012); h – Lelli et al. (2012a).

because the broad wings of their beam profiles may lead to spurious detections of diffuse emission, especially when the H I data are not cleaned down to the noise level (as is the case for the LITTLE–THINGS data cubes that are cleaned down to only 2.5σ; see Hunter et al. 2012).

Since we are interested in low column density H I emission, it is important to accurately estimate the 3σ column density sensitivity of the total H I maps. The noise in a total H I map is not uniform but varies from pixel to pixel because at each spatial position one adds a different number of channels, given that only the pixels inside a given mask are considered. Following Verheijen & Sancisi (2001), we constructed signal-to-noise ratio maps and calculated a pseudo-3σ column density contour $N_{\rm H\,I}(3\sigma)$ by averaging the values of the pixels with signal-to-noise ratio between 2.75 and 3.25. We also calculated the rms around the mean value of these pixels to estimate the uncertainty on $N_{\rm H\,I}(3\sigma)$. In particular, we halted the progressive smoothing of the H I cubes when the value of $N(3\sigma)$ was equal to 1×10^{20} cm^{-2} within the errors. The derivation of the signal-to-noise ratio maps is described in detail in Appendix A.

We calculated total H I fluxes from the smoothed maps by considering the pixels with a flux density higher than $\frac{1}{2}N_{\rm H\,I}(3\sigma)$, that can be considered as a pseudo-1.5σ contour (see Table 4). Our H I fluxes are in overall agreement with those from single-dish observations: the differences are typically $\lesssim$15 per cent apart for two objects (NGC 1569 and UGC 6456) that are affected by Galactic emission. Our smoothed H I maps, thus, recover most of the H I emission from the galaxy.

We also derived H I velocity fields by estimating an intensity-weighted mean (IWM) velocity from the masked data cube at the optimal resolution, clipping at 2σ and considering only the pixels within the pseudo-3σ contour of the total H I map. Since the H I profiles are generally broad and asymmetric, these low-resolution IWM velocity fields are uncertain and provide only an overall description of kinematics of the extended gas. For the 18 galaxies in our sample, a detailed analysis of the H I kinematics has been presented in Lelli et al. (2012a,b) and LVF14.

3 THE H I GAS IN THE OUTER REGIONS

In the following we qualitatively describe the overall properties of the H I gas in the outer regions of starburst dwarfs, while in Section 4 we quantify the outer H I asymmetry using a new asymmetry parameter; we also make a comparison with a control sample of typical star-forming Irrs and investigate the relation between outer H I distribution and starburst properties. In Section 5 we then describe each individual galaxy in detail and discuss its nearby environment.

Fig. 1 shows the total H I maps of our 18 starburst dwarfs superimposed on optical images; in each map the H I contours correspond to 1, 4, and 16 × 10^{20} atoms cm^{-2}. The outer H I distribution of starburst dwarfs shows a variety of morphologies. Several galaxies have heavily disturbed H I distributions, characterized by large-scale asymmetries, long filaments, and/or a large H I-stellar offset (NGC 4449, I Zw 18, NGC 1705, UGC 6541, NGC 1569, and I Zw 36). Other galaxies, instead, show lopsided H I morphologies, characterized by minor asymmetries and/or extensions in the outer parts (NGC 2366, NGC 4068, NGC 4214, UGC 6456, UGC 9128, UGC 4483, and SBS 1415+437). There is *not* a clear-cut separation between these two types of H I morphologies, since there are several 'intermediate' cases that have relatively regular H I distributions in the inner parts and small tails/filaments in the outer regions (NGC 4163, NGC 625, NGC 6789, and NGC 5253). We estimated the extent of the H I distribution $E_{\rm H\,I}$ by measuring the projected distance between the optical centre of the galaxy and the outermost pixel with an observed column density of 1 × 10^{20} atoms cm^{-2}. Note that $E_{\rm H\,I}$ is conceptually different from the H I radius $R_{\rm H\,I}$, as the latter is defined as the radius where the azimuthally averaged H I surface density profile (corrected for inclination) reaches 1 M$_\odot$ pc^{-2} (∼1.2 × 10^{20} atoms cm^{-2}; see e.g. Swaters et al. 2002). Since $E_{\rm H\,I}$ is *not* obtained from an azimuthal average over the total H I map, it properly takes into account anomalous extensions in the H I distribution (such as tails or filaments), but it may be affected by projection effects along the line of sight. Table 4 lists the values of $E_{\rm H\,I}$ and $E_{\rm H\,I}/R_{\rm opt}$, where the optical radius $R_{\rm opt}$ is defined as 3.2 exponential scalelengths (see LVF14) and is given in Table 1. For the 18 galaxies in our sample, $E_{\rm H\,I}/R_{\rm opt}$ ranges from ∼1.5 to ∼4,

Table 4. H I properties.

Galaxy	$S_{\rm H\,I}$ (Jy km s^{-1})	$M_{\rm H\,I}$ (10^7 M$_\odot$)	$E_{\rm H\,I}$ (arcmin)	$E_{\rm H\,I}$ (kpc)	$E_{\rm H\,I}/R_{\rm opt}$	$t_{E_{\rm H\,I}}$ (Gyr)	A
NGC 625	27.0	9.7 ± 2.2	4.7	5.4	1.6	1.1	0.60
NGC 1569	106.6	29.1 ± 4.5	10.8	10.7	3.6	1.3	0.68
NGC 1705	18.2	11.1 ± 2.9	4.0	5.9	3.9	0.5	0.74
NGC 2366	254.8	62 ± 17	10.1	9.4	2.1	1.1	0.53
NGC 4068	34.2	14.9 ± 1.6	3.6	4.5	2.5	0.7	0.52
NGC 4163	7.2	1.5 ± 0.2	2.3	2.0	2.0	1.2	0.64
NGC 4214	250.8	43 ± 8	10.4	8.2	3.7	0.6	0.52
NGC 4449	721.2	300 ± 77	34.3	42	13	7.4	0.77
NGC 5253	47.6	13.8 ± 3.4	4.6	4.7	2.2	...	0.57
NGC 6789	5.9	1.8 ± 0.3	1.8	1.9	2.7	0.2	0.60
UGC 4483	12.0	2.9 ± 0.5	2.7	2.5	4.2	0.8	0.73
UGC 6456	10.4	4.5 ± 0.5	1.9	2.4	1.9	1.5	0.51
UGC 6541	2.8	1.2 ± 0.2	1.9	2.3	2.5	...	0.73
UGC 9128	11.1	1.3 ± 0.2	1.8	1.2	2.0	0.3	0.48
UGCA 290	1.35	1.4 ± 0.2	1.1	2.1	2.3	...	0.70
I Zw 18	2.7	21 ± 4	1.6	8.5	17	1.4	0.76
I Zw 36	8.2	6.7 ± 1.3	1.9	3.3	3.7	0.7	0.64
SBS 1415+437	4.6	20.1 ± 4.6	1.8	7.3	3.0	2.5	0.42

Notes. The VLA data of NGC 4449 seem to miss diffuse H I emission (Hunter et al. 1998), thus $S_{\rm H\,I}$ and $M_{\rm H\,I}$ may be underestimated. The asymmetry parameter A is calculated using the total H I maps in Fig. 1 (see Table 3 for the relative spatial resolutions and column density sensitivities).

except for I Zw 18 ($E_{\rm H\,I}/R_{\rm opt} \simeq 17$) and NGC 4449 ($E_{\rm H\,I}/R_{\rm opt} \simeq 13$). These two objects show exceedingly extended H I tails with relatively high column densities ($\sim$1–2 $\times$ 10^{20} atoms cm^{-2}). Intriguingly, both I Zw 18 and NGC 4449 have a companion galaxy with $L_{\rm R} \simeq 0.5$–1 $\times$ 10^7 L$_\odot$ at a projected distance $\lesssim$ 10 kpc. For I Zw 18, there are strong indications that the extended H I emission is associated with the secondary body (see Lelli et al. 2012a). For NGC 4449, instead, the relation between the companion galaxy and the long H I filaments is unclear (see Martínez-Delgado et al. 2012).

Finally, we describe the H I kinematics in the outer regions. Fig. 2 shows the velocity fields of our 18 galaxies. As we stressed in Section 2, these velocity fields are only indicative due to the complex structure of the H I profiles, but they provide an overall description of the gas kinematics. For starburst dwarfs with a rotating H I disc, the outer gas generally is kinematically connected to the inner H I distribution (except for I Zw 18, discussed in Lelli et al. 2012a). This suggests that the outer discs can be regularized in a few orbital times by differential rotation. We calculated the orbital times $t_{E_{\rm H\,I}}$ at $E_{\rm H\,I}$ using the rotation velocities in Table 1 (from LVF14). These rotation velocities are typically estimated at $\sim$1–2 $R_{\rm opt}$, thus we are extrapolating their values to larger radii by assuming that the rotation curve is flat and the outer gas lies approximately in the same plane as the inner H I disc. The values of $t_{E_{\rm H\,I}}$ in Table 4, therefore, should be considered as *order-of-magnitude* estimates. Despite these uncertainties, the orbital times at $E_{\rm H\,I}$ are consistently of the order of $\sim$0.5–1 Gyr (except for NGC 4449 with $t_{E_{\rm H\,I}} \simeq 7$ Gyr), indicating that the outer asymmetries must be relatively recent and possibly short-lived.

4 QUANTIFYING THE H I ASYMMETRY

4.1 The asymmetry parameter

To investigate the relation between the H I morphology and the starburst, it is desirable to quantify the degree of asymmetry/lopsidedness in the outer H I distribution of each individual galaxy. The infrared/optical morphologies of galaxies are usually quantified using the concentration–asymmetry–smoothness (CAS) parameters (Conselice 2003) and the Gini–M_{20} parameters (Lotz, Primack & Madau 2004). Recently, Holwerda et al. (2011a,b, 2013) used these parameters to quantify the H I morphologies in several samples of nearby galaxies. In particular, Holwerda et al. (2011b) used total H I maps from the WHISP survey, and found that the CAS and Gini parameters only weakly correlate with previous *visual* classifications of morphological lopsidedness (by Swaters et al. 2002; Noordermeer et al. 2005). Holwerda et al. (2011a,b) defined the asymmetry parameter $\mathcal{A}$ as

$$\mathcal{A} = \frac{\sum_{i,\,j} |I(i,\,j) - I_{180^\circ}(i,\,j)|}{\sum_{i,\,j} |I(i,\,j)|}, \tag{1}$$

where $I(i,j)$ and $I_{180^\circ}(i,\,j)$ are the flux densities at position (i,j) in the original image and in an image rotated by 180° with respect to the galaxy centre, respectively. This definition normalizes the residuals between the original image and the rotated image to the *total* flux. Thus, asymmetries in the outer regions may have negligible weight in the sum, since the flux densities in the outer parts can be up to $\sim$2 orders of magnitude lower than those in the inner parts. This effect has been pointed out by Holwerda et al. (2013) (see their section 3.2 and fig. 2), who demonstrated that the value of $\mathcal{A}$ does not strongly depend on the outer H I emission observed in low-resolution H I maps. Our goal, instead, is to give weight to the large-scale asymmetries in the outer parts. Thus, we use a new definition of A:

$$A = \frac{1}{N} \sum_{i,j}^{N} \frac{|I(i,\,j) - I_{180^\circ}(i,\,j)|}{|I(i,\,j) + I_{180^\circ}(i,\,j)|}, \tag{2}$$

where N is the total number of pixels in the image. This definition normalizes the residuals at position (i,j) to the *local* flux density. In particular, if H I emission is detected only on one side of the galaxy, the residuals at (i,j) and $(i,\,j)_{180^\circ}$ get the maximum value (=1).

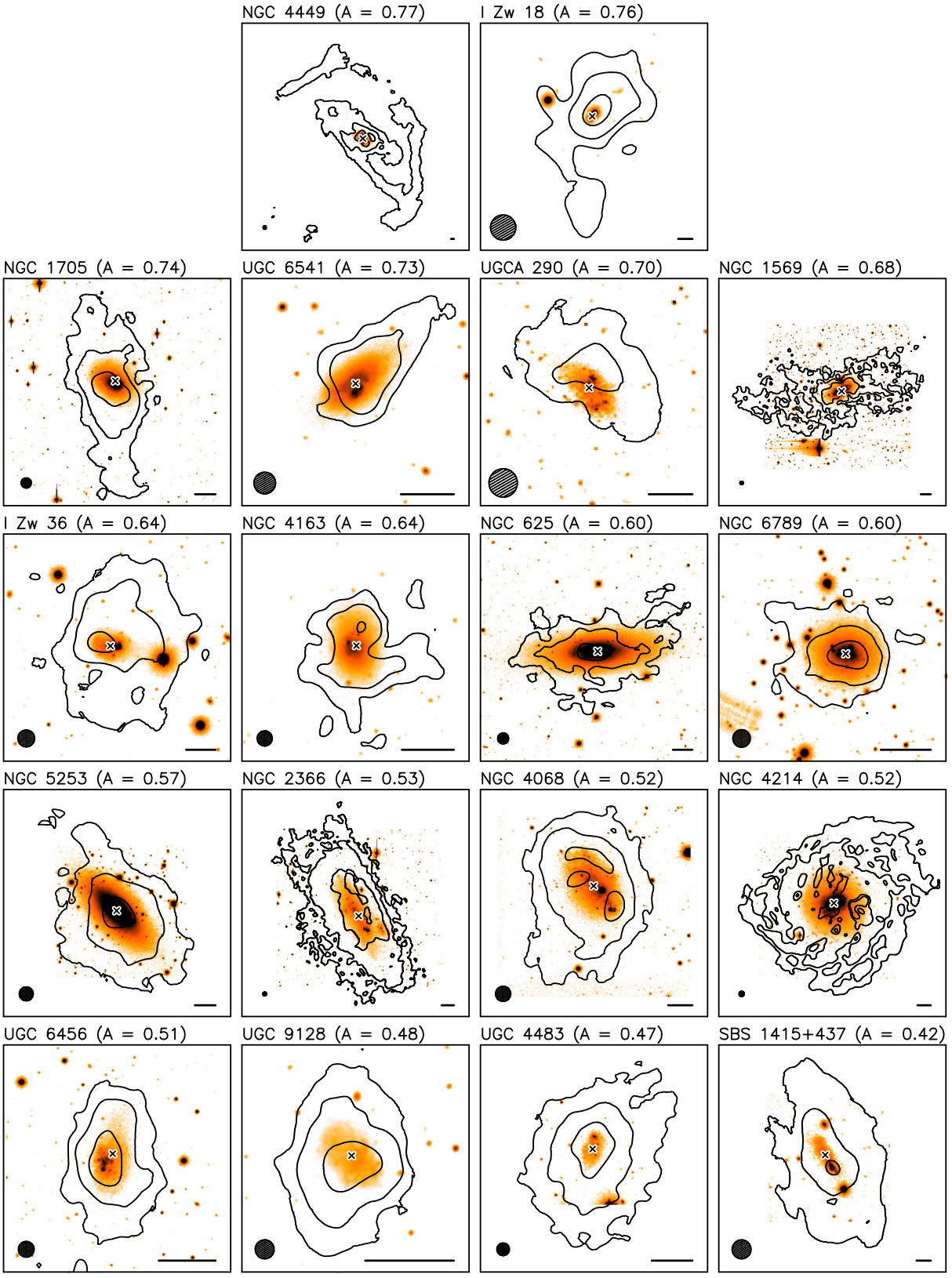

Figure 1. Total H I maps superimposed on optical images. The galaxies are ordered according to the value of the asymmetry parameter A (see Section 4 for details). The contours are at 1, 4, 16 $\times$ 10^{20} atoms cm^{-2}. The cross shows the optical centre. The ellipse to the bottom-left shows the H I beam (given in Table 3). The bar to the bottom-right corresponds to 1 kpc. Please see the electronic version of the journal for a colour version of this figure.

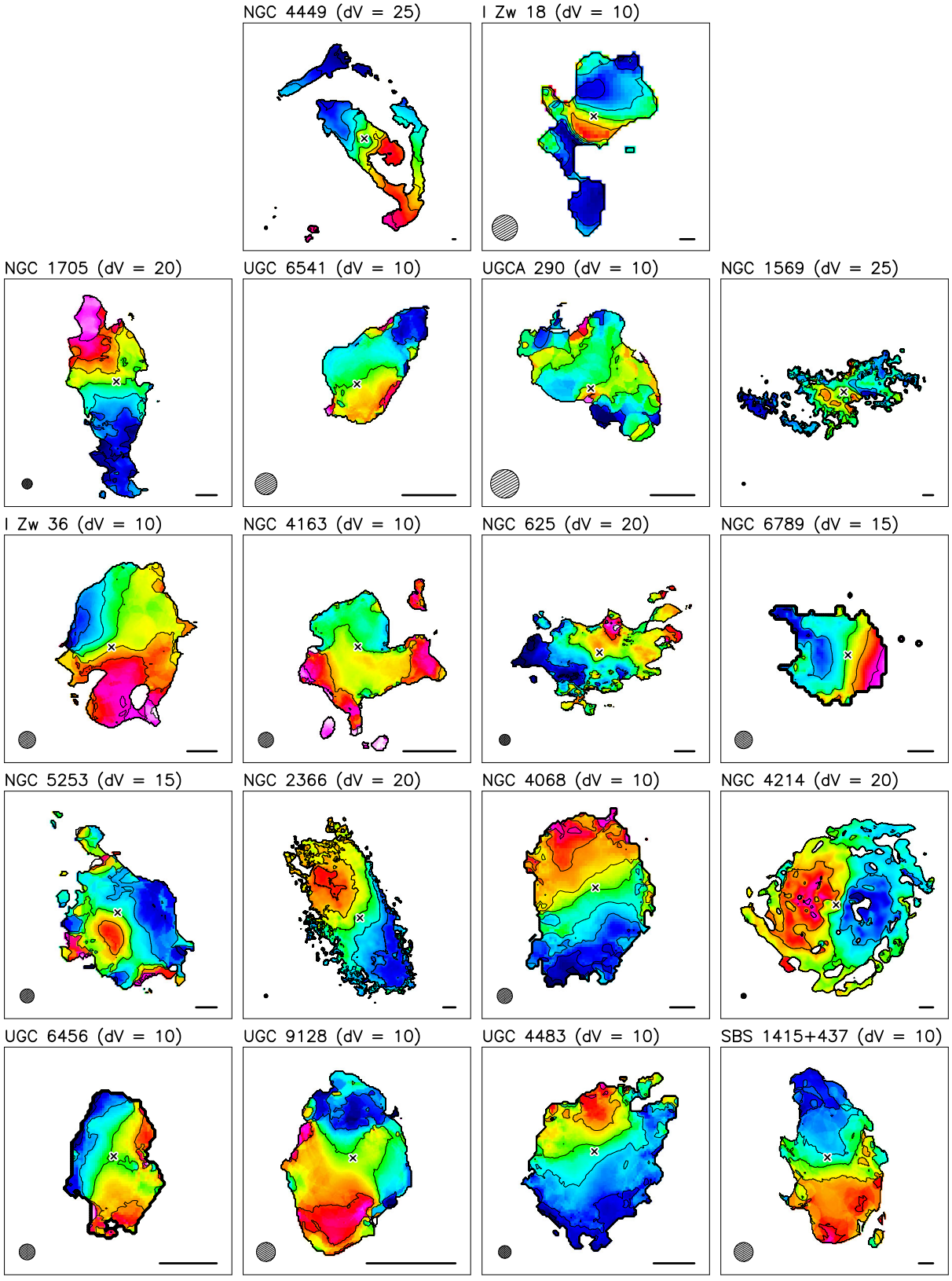

Figure 2. H I velocity fields. The box sizes are the same as in Fig. 1. The velocity separation dV between the contours is indicated. The cross shows the optical centre. The ellipse to the bottom-left shows the H I beam (given in Table 3). The bar to the bottom-right corresponds to 1 kpc. Please see the electronic version of the journal for a colour version of this figure.

In Fig. 1 the total H I maps of our 18 starburst dwarfs are ordered according to the value of A. It is clear that our definition of A reliably quantifies the H I asymmetry in the outer parts. The value of A, however, may depend on (i) the assumed galaxy centre, (ii) the column density sensitivity of the H I observations, and (iii) the spatial resolution in terms of both the beam size in kpc and the relative number of beams across the H I map. In the following, we describe the effects of these factors on the value of A.

We adopted the optical centres derived in LVF14 by fitting ellipses to the outer isophotes (see Table 1). We did not consider the *kinematic* centres because 50 per cent of the galaxies in our sample have either a kinematically disturbed H I disc or an unsettled H I distribution, thus the kinematic parameters are either very uncertain or undefined. Moreover, the use of the optical centre returns high values of A for galaxies that show a strong offset between the H I distribution and the stellar body (e.g. NGC 1705 and UGCA 290), that may indicate a recent interaction/accretion event. We checked that small changes in the value of the centres ($\sim$2 arcsec) do not significantly affect the value of A (the absolute differences in A are $\lesssim$0.05). This is expected because (i) the typical uncertainties on the position of the optical centre ($\sim$1–2 arcsec) are much smaller than the H I beam ($\gtrsim$20 arcsec), and (ii) by our definition of A, high column density asymmetries in the inner parts do not have much weight.

Regarding the column density sensitivity, the values of A in Fig. 1 and Table 4 have been calculated considering only pixels with $N_{\rm H\,I} \geq 10^{20}$ cm^{-2}, since this corresponds to the pseudo-3σ contour of our total H I maps (see Section 2 and Appendix A). To test the effect of this column density threshold, in Fig. 3 (top) we compare the values of A obtained by considering thresholds of 1 and 2 $\times$ 10^{20} cm^{-2}. The differences in A are within $\sim$0.1 and do not show a systematic trend, implying that the detailed shape of the outermost contour in the total H I map does not strongly affect the value of A. We warn, however, that the use of a column density threshold provides reliable results as long as (i) one does *not* consider values much below the pseudo-3σ contour, introducing noise in the total H I maps, and (ii) one does *not* consider high column density thresholds (e.g. $N_{\rm H\,I} \gtrsim 5{-}10 \times 10^{20}$ cm^{-2}), probing the small-scale clumpiness of the H I distribution. We also note that, when using a fixed column density threshold for different galaxies, the inclination i of the H I disc may introduce some systematic effects, given that *projected* column densities correspond to different *face-on* surface densities. For an optically thin H I disc, the projected column density increases with $1/\cos(i)$. Thus, inclination effects on the column density threshold become important only in edge-on discs with $i \gtrsim 70^{\circ}$, for which projected column densities of $\sim 1 \times 10^{20}$ cm^{-2} would correspond to face-on surface densities that are lower by a factor of $\gtrsim$3. In our galaxy sample, the inclinations of the H I discs are $\lesssim 70^{\circ}$ (see LVF14), thus projection effects are not a serious concern here.

The spatial resolution of the H I observations deserves some attention in the derivation of A. To quantify the effects of beam smearing, we constructed total H I maps at 20 and 30 arcsec resolution for all the galaxies in our sample (except for NGC 4449 that has H I data at a native resolution of $\sim$60 arcsec). The respective values of A, calculated using a threshold of 1 $\times$ 10^{20} cm^{-2}, are compared in Fig. 3 (bottom panel). As expected, total H I maps at higher resolutions systematically yield higher values of A. The differences in A, however, appear reasonably small (within 0.1). Galaxies with a small number of beams along the major axis of the H I disc (e.g. NGC 4163, NGC 6789, and I Zw 18) typically show the largest differences in A ($\sim$0.1), whereas galaxies with well-resolved H I maps (e.g. NGC 2366, NGC 1569, and NGC 4214) show very small differences ($\lesssim$0.03). For the latter galaxies, a severe smoothing of the H I data down to 60 arcsec (a factor of 3) would still give differences in $A \lesssim 0.1$. Thus, we draw the following conclusions: (i) to have a reliable estimate of A, one needs at least $\sim$5 resolution elements along the major axis of the total H I map, and (ii) when the previous condition is met, differences in spatial resolution by a factor of $\sim$3 give relatively small differences in A ($\lesssim$0.1). Our total H I maps are all reasonably resolved (see Fig. 1) and have linear resolutions ranging from $\sim$0.3 to $\sim$0.7 kpc (see Table 3), thus it makes sense to compare the values of A for different galaxies. Exceptions are NGC 4449, I Zw 18, and SBS 1415+437 that have total H I maps with linear resolutions $\gtrsim$1 kpc. Despite the low linear resolution, NGC 4449 and I Zw 18 show the highest values of A in our sample, indicating that data at higher resolutions would only increase the difference with the other galaxies. On the contrary, SBS 1415+437 has the lowest value of A in our sample; this may be an effect of beam smearing. We did not build total H I maps at the same linear resolution (in kpc) for all the galaxies because it is not possible to find a compromise between the required number of beams along the H I major axis ($\gtrsim$5 in order to have a proper estimate of A) and

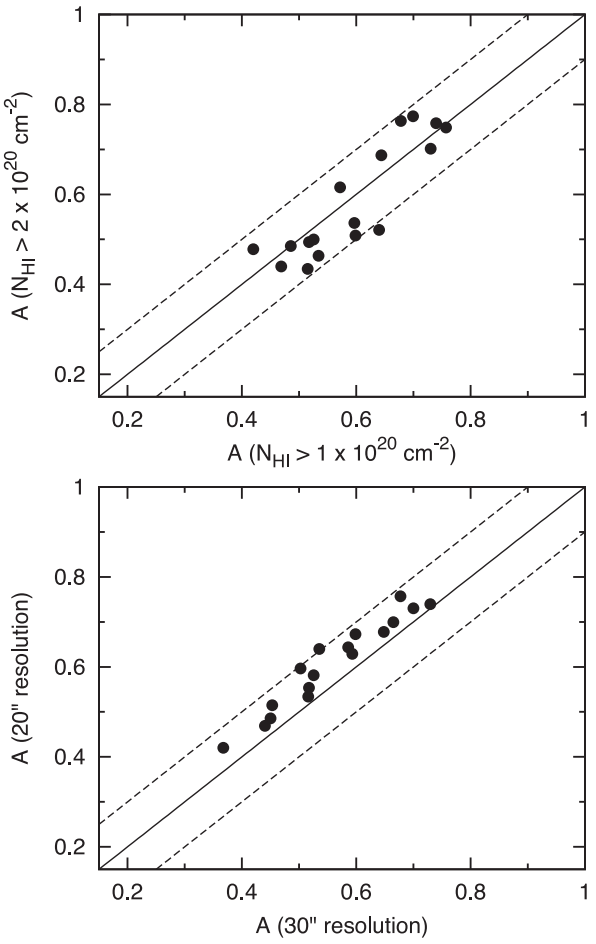

Figure 3. Testing the dependence of the asymmetry parameter A on the column density threshold (top) and on the spatial resolution of the total H I maps (bottom). In the top panel, dots show the values of A obtained from the total H I maps in Fig. 1 using a column density threshold of 1 and 2 $\times$ 10^{20} atoms cm^{-2}. In the bottom panel, dots show the values of A using H I maps at 20 and 30 arcsec (keeping the column density threshold fixed to 10^{20} atoms cm^{-2}). The solid line corresponds to a null variation in the value of A, whereas the dashed lines correspond to variations of $\pm$0.1. See Section 4.1 for details.

the 3σ column density sensitivity ($\lesssim 1 \times 10^{20}$ in order to probe the outer H I emission).

4.2 Comparison with typical irregulars

In this section, we estimate A for a control sample of typical star-forming Irrs and make a comparison with our sample of starburst dwarfs. We use total H I maps from the VLA-ANGST survey (Ott et al. 2012), which provides multiconfiguration VLA observations for 29 low-mass galaxies from ANGST (Dalcanton et al. 2009). In order to have two galaxy samples that span similar ranges of stellar and H I masses, we exclude eight objects with $M_B \lesssim -11$ (nearly equivalent to $M_* \lesssim 10^7\,M_\odot$), given that such very low mass galaxies are not present in our sample of starburst dwarfs. We also exclude AO 0952+69 (Arp's loop) that may be a feature in the spiral arm of M81 (Ott et al. 2012) or a tidal dwarf galaxy (Weisz et al. 2011). The VLA-ANGST sample also contains three starburst dwarfs that are included in our sample (NGC 4163, UGC 4483, and UGC 9128), which we use to test the consistency between our total H I maps and the VLA-ANGST ones. The control sample of typical Irrs, therefore, contains 17 galaxies.

The starburst and control samples cover similarly broad ranges of absolute magnitudes ($-12 \lesssim M_B \lesssim -18$) and H I masses ($10^7 \lesssim M_{HI}/M_\odot \lesssim 10^9$). For the starburst sample, the mean values in M_B and M_{HI} are, respectively, -14.9 mag and $3.0 \times 10^8\,M_\odot$, while for the control sample they are -13.9 mag and $1.1 \times 10^8\,M_\odot$. Despite the starburst dwarfs are, on average, slightly more luminous and gas rich than the typical Irrs, it is clear that the two samples can be properly compared. Moreover, similarly to the starburst dwarfs in our sample, the VLA-ANGST galaxies have been resolved into single stars by *HST* (Dalcanton et al. 2009). For most of these galaxies, Weisz et al. (2011) derived SFHs by averaging the SFR over a single time bin in the last $\sim$1 Gyr, thus we cannot check whether they have a recent birth rate parameter $b \lesssim 3$, confirming that they are *not* starburst dwarfs. However, as far as we are aware of, the 17 galaxies in our control sample do not show any sign of recent starburst activity either in their CMDs or in their integrated spectra, thus we consider them representative for typical star-forming Irrs. The natural-weighted H I maps from VLA-ANGST have both an adequate number of resolution elements along the H I major axis and a 3σ column density sensitivity $\lesssim 10^{20}\,cm^{-2}$ (see Ott et al. 2012), thus we can safely calculate A using a column density threshold of $10^{20}\,cm^{-2}$ (as for our starburst dwarfs). The beam sizes of these H I maps range from $\sim$60 to $\sim$200 pc, significantly smaller than those of our own H I maps (cf. with Table 3). As we discussed in Section 4.1, this implies that the values of A for our starburst dwarfs may be systematically *underestimated* with respect to those of the VLA-ANGST Irrs. For UGC 4483 and UGC 9128, however, the VLA-ANGST H I maps and our total H I maps yield remarkably consistent results: UGC 4483 has $A = 0.469$ from our map and $A = 0.464$ from the VLA-ANGST one, while UGC 9128 has $A = 0.485$ from our map and $A = 0.480$ from the VLA-ANGST one. NGC 4163, instead, shows a significant discrepancy: our map yields $A = 0.64$ while the VLA-ANGST one returns $A = 0.50$. The VLA-ANGST map of NGC 4163 does not trace the full extent of the H I tail to the west and does not detect the cloud complexes to the south (compare our Fig. 1 with fig. 1 8 of Ott et al. 2012). This is likely due to a different masking of the H I emission during the derivation of the total H I map. We are confident that these H I features are real given that they have been detected also by Swaters et al. (2002) using WSRT data. Fig. 4 shows that starburst dwarfs systematically have *higher* values of A than typical Irrs. The mean and median values

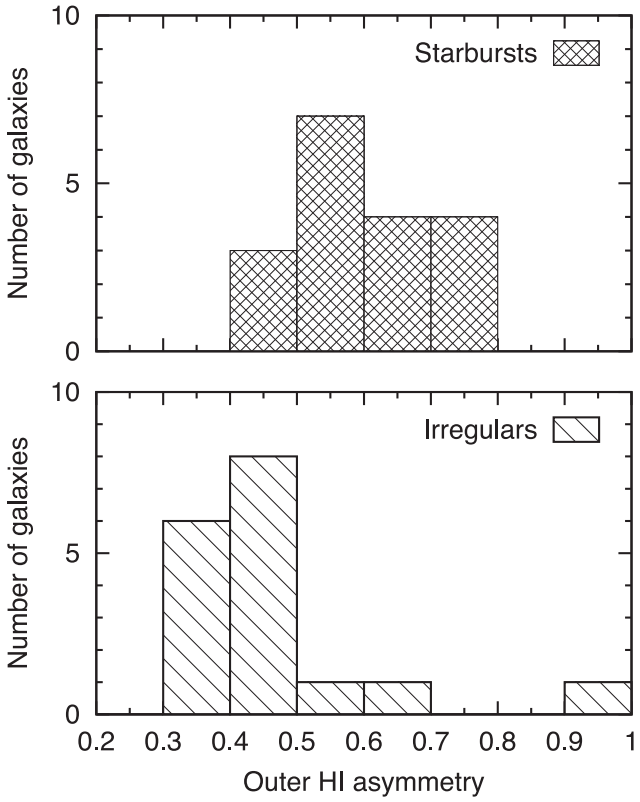

Figure 4. The asymmetry parameter A for our sample of 18 starburst dwarfs and for a control sample of 17 typical Irrs, drawn from the VLA-ANGST survey. Starburst dwarfs clearly have more asymmetric H I morphologies in the outer parts than typical Irrs of similar masses. See Section 4.2 for details.

of these distributions are, respectively, 0.60 and 0.60 for the sample of starburst dwarfs, and 0.47 and 0.41 for the control sample of Irrs. Since the total H I maps of starburst dwarfs have larger beam sizes than those of Irrs, the difference between the two samples may be even larger. Given the possible effects of beam smearing on A, we did not perform a statistical analysis of the two distributions (e.g. using a Kolmogorov–Smirnoff test). It is clear, however, that starburst dwarfs generally have more asymmetric H I morphologies in their outer regions than typical Irrs.

Two galaxies from the control sample have very high values of A, comparable with those of the most disturbed starburst dwarfs. These objects are NGC 404 ($A = 0.67$) and DDO 6 ($A = 1$). NGC 404 is at the high-mass end of the dwarf classification ($M_B \simeq -16.2$) and shows an unusual lenticular morphology for a dwarf galaxy. Several authors (e.g. Thilker et al. 2010) argued that NGC 404 may have experienced a merger in the last $\sim$1 Gyr given that it has an inner, counter-rotating stellar core (Bouchard et al. 2010) and an outer, extended H I ring (del Río, Brinks & Cepa 2004) hosting recent, low-level star formation (Thilker et al. 2010). Considering these facts, the relatively high value of A is not surprising, and demonstrates that our definition of A can successfully identify past interacting/merging systems. Regarding DDO 6, both Skillman, Côté & Miller (2003) and Weisz et al. (2011) classified this object as a 'transition' dwarf, i.e. a low-mass galaxy with detected H I emission but little or no Hα flux (Mateo 1998). In DDO 6, H I emission is detected only on one side of the galaxy (similarly to UGC 6541 in our sample), hence this object has an extremely high value of A. It would be interesting to investigate whether this galaxy has experienced a recent starburst. Intriguingly, the well-studied 'transition' dwarf Antlia has been

classified as a starburst by McQuinn et al. (2012), and has a H I distribution similar to DDO 6 and UGC 6541 (see Ott et al. 2012; Antlia is not included here because it has $M_B \lesssim -11$).

4.3 H I asymmetries versus starburst properties

We now investigate the possible relations between A and the properties of the starburst as derived from the *HST* studies of the resolved stellar populations. We consider the following quantities (see Table 2):

(i) the birth rate parameter $b = \mathrm{SFR_p}/\overline{\mathrm{SFR}}$, where $\mathrm{SFR_p}$ is the peak SFR over the past 1 Gyr and $\overline{\mathrm{SFR}}$ is the average SFR over the past 6 Gyr (see McQuinn et al. 2010);

(ii) the peak SFR surface density $\Sigma_{\mathrm{SFR}}(t_p) = \mathrm{SFR_p}/(\pi R^2_{\mathrm{opt}})$, where R_{opt} is defined as 3.2 exponential scalelengths (see LVF14);

(iii) the present-day SFR surface density $\Sigma_{\mathrm{SFR}}(0) = \mathrm{SFR_0}/(\pi R^2_{\mathrm{opt}})$, where $\mathrm{SFR_0}$ is the average SFR over the last 10 Myr;

(iv) the specific SFR (sSFR) calculated both as $\mathrm{SFR_0}/M_*$ and as $\mathrm{SFR_p}/M_*$;

(v) the lookback time t_p at $\mathrm{SFR_p}$.

In particular, t_p can be considered as the typical 'age' of the starburst, allowing us to distinguish between 'old' bursts (with $t_p \gtrsim 100$ Myr) and 'young' bursts (with $t_p \lesssim 100$ Myr). The SFHs of five galaxies (NGC 2366, NGC 4068, UGC 4483, UGC 9128, and SBS 1415+437) show two distinct peaks with similar SFRs (consistent within 1σ). In these cases, we consider the SFR and the lookback time of the older peak since this is the one that formed more stars, given that the SFR is averaged over a larger time bin (typically a factor of ∼4; see McQuinn et al. 2010). For UGC 6541 and I Zw 36, the recent SFH is not well constrained (see Schulte-Ladbeck et al. 2000, 2001), thus we have no robust estimate of $\Sigma_{\mathrm{SFR}}(t_p)$, $\mathrm{sSFR_p}$, and t_p.

In Fig. 5, we plot A versus the SFR indicators $\Sigma_{\mathrm{SFR}}(0)$, $\Sigma_{\mathrm{SFR}}(t_p)$, sSFR(0), and sSFR($t_p$). To quantify possible trends in these diagrams, we calculated the Pearson's correlation coefficient ρ_{cc}, where $\rho_{cc} = \pm 1$ for an ideal linear correlation/anticorrelation, whereas $\rho_{cc} \simeq 0$ if no correlation is present. We found values of $\rho_{cc} \simeq 0.3$–0.4, except for the A–$\Sigma_{\mathrm{SFR}}(t_p)$ diagram that yields $\rho_{cc} \simeq 0.6$. We think that this weak trend is *not* significant because it is driven by three galaxies (NGC 4449, I Zw 18, and NGC 1705) that have $t_p \simeq 10$ Myr: for these objects the values of $\Sigma_{\mathrm{SFR}}(t_p) \simeq \Sigma_{\mathrm{SFR}}(0)$ may be systematically enhanced with respect to galaxies with older bursts because the SFR is averaged over a smaller time bin (∼10 Myr versus ∼50–100 Myr), given that the intrinsic time resolution of the SFHs increase with decreasing lookback time (see e.g. McQuinn et al. 2010). We also found no clear correlation with b.

Fig. 6 (left) shows that a clear trend is present between A and t_p ($\rho_{cc} \simeq -0.7$): galaxies hosting a 'young' burst generally have a more asymmetric H I distribution than galaxies hosting an 'old' one, further suggesting a close link between the outer, disturbed gas morphology and the central, recent starburst activity. Galaxies with minor asymmetries ($A \lesssim 0.6$) have values of $t_p \simeq 500$ Myr (apart from UGC 6456), which are comparable within a factor of ∼2 with

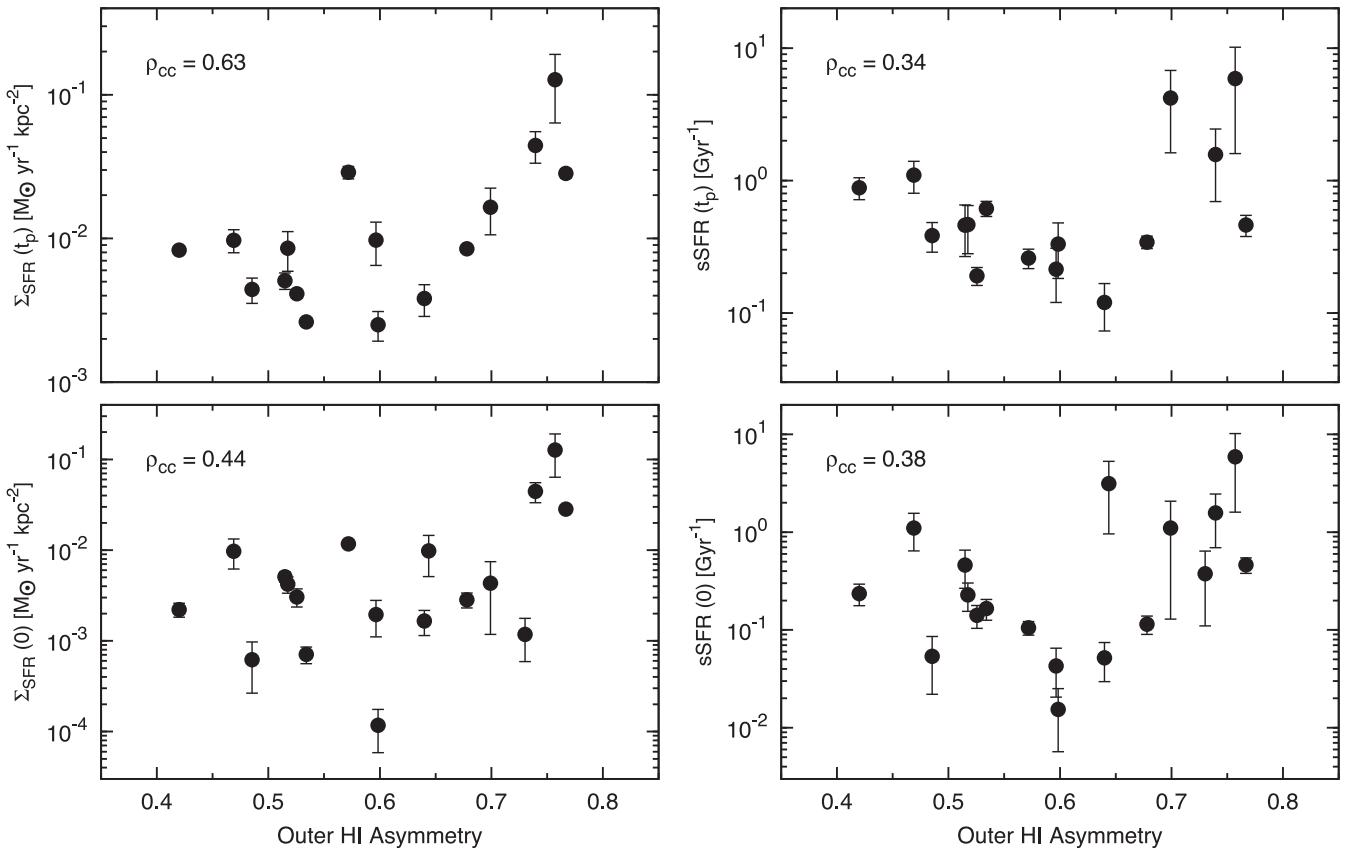

Figure 5. The asymmetry parameter A versus the peak SFR surface density $\Sigma_{\mathrm{SFR}}(t_p)$ (top-left), the present-day SFR surface density $\Sigma_{\mathrm{SFR}}(0)$ (bottom-left), the peak specific SFR (top-right), and the present-day specific SFR (bottom-right). In each diagram, the value of the Pearson's correlation coefficient is indicated. See Section 4.3 for details.

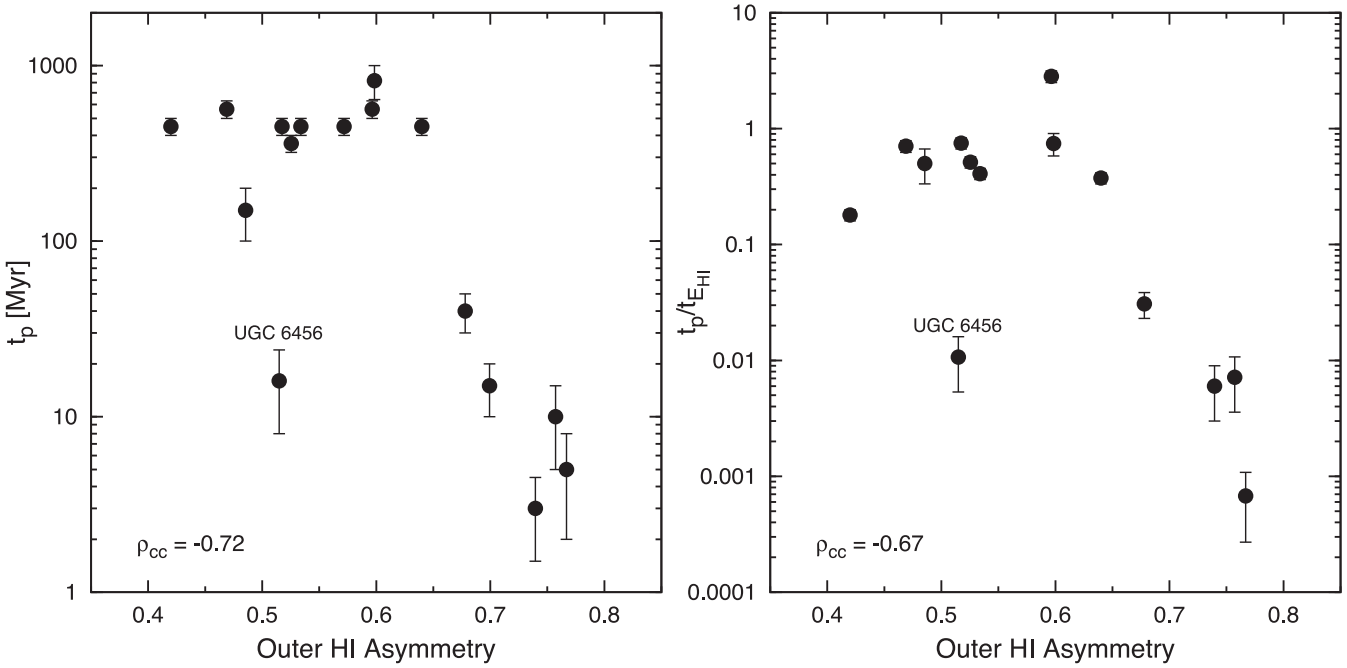

Figure 6. The asymmetry parameter A versus the lookback time t_p at the peak of the SFH (left) and the ratio $t_p/t_{E_{H\,I}}$ (right), which roughly estimates the number of orbits that the outermost gas has completed since the onset of the starburst. In both panels, the value of the Pearson's correlation coefficient is indicated. See Section 4.3 for details.

the orbital times $t_{E_{H\,I}}$ at the outermost radii $E_{H\,I}$. This is shown in Fig. 6 (right), where we plot A against the ratio $t_p/t_{E_{H\,I}}$. We recall that $t_{E_{H\,I}}$ is an order-of-magnitude estimate, thus the ratio $t_p/t_{E_{H\,I}}$ provides only a rough measure of the number of orbits that the outer gas may have completed since the epoch of the most intense star formation activity. Despite these uncertainties, Fig. 6 (right) clearly indicates that galaxies hosting an 'old' burst may have had enough time to complete an entire revolution around the centre and, thus, regularize their outer H I distribution.

Finally, we discuss the 'outlier' UGC 6456 (VII Zw 403) indicated in Fig. 6. This galaxy has been recently studied by Simpson et al. (2011), who pointed out the relatively regular H I morphology and the lack of a clear external trigger. The total H I map and velocity field of Hunter et al. (2012), however, show a tail/extension to the south-west. We also detected this feature in our total H I map, but it is below the 3σ column density sensitivity of the observations, having $N_{H\,I} \lesssim 5 \times 10^{19}$ cm^{-2}. Deeper H I observations are needed to confirm whether this H I tail is real. The location of UGC 6456 in Figs 5 and 6 would change if one adopts column density thresholds $\lesssim 5 \times 10^{19}$ cm^{-2}, but unfortunately these low values cannot be consistently adopted here due to the limited sensitivity of the H I observations for several galaxies in our sample.

5 INDIVIDUAL GALAXIES AND THEIR ENVIRONMENT

In the following, we discuss in detail the H I properties of individual galaxies in our sample and describe their nearby environment. We used the NASA/IPAC Extragalactic Database (NED)[1] to search for nearby objects with measured systemic velocities within ± 300 km s^{-1} with respect to the starburst dwarf. Table 5 provides the three nearest galaxies to each starburst dwarf, together with their basic properties (from Karachentsev, Makarov & Kaisina 2013). We checked that these objects are actual galaxies by visual inspection, and excluded background/foreground galaxies when accurate, redshift-independent distances were available. Since most of the starburst dwarfs considered here have distances $D \lesssim 7$ Mpc, Table 5 should be nearly complete down to dwarf galaxies with total magnitudes $M_B \simeq -11$ and mean surface brightnesses $\mu_B \simeq 25$ mag arcsec^{-2} (cf. with Karachentsev et al. 2004, 2013). SBS 1415+437 and I Zw 18, however, are at a distance of $\sim$14 and $\sim$18 Mpc, respectively, thus they may have faint companions that have not been identified by optical surveys. An object with a peculiar velocity of $\sim$200 km s^{-1} covers $\sim$200 kpc in $\sim$1 Gyr, thus it is possible that a galaxy at a projected distance $D_p \lesssim 200$ kpc from a starburst dwarf might have triggered the burst by a *past collision* on an hyperbolic orbit (e.g. Noguchi 1988). Most of the galaxies in our sample have such a potential perturber, except for NGC 1705, NGC 6789, and UGC 9128. We stress, however, that the presence of such a companion does not guarantee that the starburst has been triggered by a past collision, given that the relative orbits of the two galaxies are unknown.

NGC 625 has a $\sim$2 kpc H I tail to the north-west that shows a coherent kinematic structure at $V_{los} \simeq 420$ km s^{-1}. A second tail/extension is present to the south-east, but it does not show a clear kinematic structure. Our total H I map and velocity field are in close agreement with those from Côté, Carignan & Freeman (2000) and Cannon et al. (2004). NGC 625 is part of the Sculptor group, but it is quite far from the central, massive galaxy NGC 253, being at a projected distance of $\sim$1.3 Mpc (Karachentsev 2005).

NGC 1569 has a heavily disturbed H I distribution. A H I cloud with $M_{H\,I} \simeq 2 \times 10^7$ M$_\odot$ lies at $V_{los} \simeq -150$ km s^{-1} to the east of the galaxy, and is connected to the main H I distribution by a

[1]NED is operated by the Jet Propulsion Laboratory, California Institute of Technology, under contract with the National Aeronautics and Space Administration.

thin bridge (see also Stil & Israel 1998). The data cube is strongly affected by Galactic emission, thus the total H I map and the velocity field are uncertain. Our results are in close agreement with those from Stil & Israel (1998, 2002) and Johnson et al. (2012). NGC 1569 is part of the IC 432 group (Grocholski et al. 2008) and has a nearby companion (UGCA 92) at a projected distance of ∼70 kpc with a similar systemic velocity (within ∼20 km s^{-1}).

NGC 1705 has an extended, warped H I disc. The H I disc shows relatively regular morphology and kinematics, but it is strongly offset with respect to the stellar component: the optical and kinematic centres differ by ∼550 pc, while the optical and kinematic PAs differ by ∼45° (see LVF14). To the north-east, there is also a small H I extension with peculiar kinematics that may be associated with the Hα wind (see Meurer, Staveley-Smith & Killeen 1998; Elson,

Table 5. Environment of the starburst dwarfs in our sample. We used information from NED to calculate the projected distances D_p from the nearest galaxies and the difference between their respective systemic velocities ΔV_{sys}. The properties of the nearest galaxies are taken from Karachentsev et al. (2013), and given only when their distances are estimated from the TRGB (the distance of NGC 2403 is estimated from Cepheids). Objects without an accurate distance estimate may be background/foreground galaxies. The properties of I Zw 18 C are taken from Lelli et al. (2012a). The morphological types are taken from NED and/or Karachentsev et al. (2013).

Galaxy	Membership	Nearest galaxies	D_p (kpc)	ΔV_{sys} (km s^{-1})	Type	Dist (Mpc)	M_B (mag)	log($M_{H\,I}$) ($M_\odot$)	$W_{50,\,H\,I}$ (km s^{-1})
NGC 625	Sculptor group	ESO 245−005	203	−7	Im	4.4	−15.6	8.58	60
	(periphery)	CFC97 Sc 24[a]	402	−236	...	...	...	...	92
		GSD 106	619	132	...	...	...	...	...
NGC 1569	IC 432 group	UGCA 92	74	19	Irr	3.0	−15.6	8.17	56
		Cam B	190	157	Irr	3.3	−11.9	7.08	21
		UGCA 86	231	147	Im?	3.0	−17.9	...	...
NGC 1705	Field	LSBG F157−089[b]	518	175	...	...	...	...	...
		MRSS 157−121650[c]	562	−50	...	...	...	...	...
		SGC 0409.0−5638	631	242	Irr	...	...	...	...
NGC 2366	M81 group	NGC 2363[d]	2	−33	Irr	...	...	...	...
	(periphery)	UGCA 133[e]	133	110	Sph	3.2	−12.1	<6.0	...
		NGC 2403	206	30	Scd	3.2	−19.2	9.48	240
NGC 4068	CVn I cloud	MCG +09−20−131	135	−47	Irr	4.6	−13.1	7.37	27
		ASK 185765.0[f]	143	291	...	...	...	...	...
		UGC 7298	145	−33	Irr	4.2	−12.3	7.28	21
NGC 4163	CVn I cloud	MCG +06−27−017[g]	27	181	Im	4.8	−13.0	...	...
		NGC 4190	29	70	Im/BCD	2.8	−13.9	7.46	49
		DDO 113	30	126	Sph?	2.9	−11.5	<5.56	32
NGC 4214	CVn I cloud	DDO 113	8	−7	Sph?	2.9	−11.5	<5.56	...
		NGC 4190	23	−63	Im/BCD	2.8	−13.9	7.46	49
		NGC 4163	34	−133	BCD	3.0	−13.8	7.16	32
NGC 4449	CVn I cloud	DDO 125	44	−15	Im	2.7	−14.3	7.48	27
		MCG +07−26−012	77	226	Im	...	...	...	...
		DDO 120	155	252	Im	...	...	...	...
NGC 5253	M83 group	ESO 444−084[h]	54	116	Sc	...	...	...	...
		NGC 5264	108	68	Im	4.5	−15.9	7.65	35
		HIDEEP J1337−33	111	181	Irr	4.4	−11.1	6.67	20
NGC 6789	Local Void	ABELL 2312:[MPC97] 04[i]	297	59	...	...	...	...	...
		UGC 11411	400	220	BCD	...	...	...	...
		LEDA 166193	578	290	Irr	...	...	...	28
UGC 4483	M81 group	M81 Dwarf A	92	−45	Irr	3.5	−11.5	7.06	21
		Holmberg II	100	−16	Im	3.4	−16.7	8.61	64
		DDO 53	201	−138	Irr	3.6	−13.4	7.62	30
UGC 6456	M81 group	CGCG 351−049[j]	151	8	...	...	...	...	...
	(periphery)	UGC 8245[j]	358	172	Im	...	...	...	...
		DDO 82	683	158	Im	4.0	−14.7	...	...
UGC 6541	CVn I cloud	ASK 184683.0	213	208	...	...	...	...	...
	(periphery)	ASK 185765.0[f]	289	247	...	...	...	...	...
		NGC 3741	292	−21	Im/BCD	3.0	−13.1	7.88	83
UGC 9128	Field	LSBG F650−01[k]	353	−167	...	...	...	...	...
		MAPS O-383-0548118[l]	359	−93	...	...	...	...	...
		SDSS J145657.7+221315[l]	365	−102	...	...	...	...	...
UGCA 290	NGC 4631 group?	UGC 7719	83	210	Sdm	...	...	...	57
		IC 3687	115	114	Im	4.6	−14.6	7.90	36
		BTS 142	122	251	Irr	...	...	...	23
I Zw 18	Field	I Zw 18 C	2	−16	Irr	18.2	−12.1	$\lesssim$8.08	∼45
		ASK 153750.0	639	243	...	...	...	...	...
		MGC +09−16−029	1052	−159	...	...	...	...	...

Table 5 – *continued*

Galaxy	Membership	Nearest galaxies	D_p (kpc)	ΔV_{sys} (km s^{-1})	Type	Dist (Mpc)	M_B (mag)	$\log(M_{H\,I})$ ($M_\odot$)	$W_{50,\,H\,I}$ (km s^{-1})
I Zw 36	CVn I cloud	UGC 7639[m]	117	105	Im	...	...	...	...
		NGC 4248[n]	183	207	...	...	...	...	...
		MAPS O−171−0165792	214	195	...	...	...	...	...
SBS 1415+437	Field	MAPS O−221−0093662	179	105	...	...	...	...	...
		ASK 310753.0	492	18	...	...	...	...	...
		NGC 5608	493	47	Im	...	...	...	...

[a] According to Karachentsev et al. (2004), this galaxy is not in the Sculptor group but lie outside the Local Volume. The value of $W_{50,\,H\,I}$ is taken from Cote et al. (1997).
[b] This galaxy may be in the Dorado group ($D \simeq 17$ Mpc; Firth et al. 2006).
[c] This object may be an ultracompact dwarf in the Dorado group ($D \simeq 17$ Mpc; Evstigneeva et al. 2007).
[d] It is unclear whether this object is part of NGC 2366 or a separate galaxy (see Fig. 7).
[e] The systemic velocity of this galaxy is not reported by NED. We used the value given by Karachentsev et al. (2013).
[f] Trentham, Tully & Verheijen (2001) included this galaxy in their study of the Ursa Major cluster. However, ASK 185765.0 is probably not a cluster member, given that its systemic velocity is ∼497 km s^{-1} (from the Sloan Digital Sky Survey).
[g] This galaxy is close to NGC 4163 on the sky, but inhabits a further region of the CVn I cloud having $D \simeq 4.8$ Mpc (from the TRGB).
[h] This edge-on spiral is not a member of the M83 group and probably is a background galaxy.
[i] NED classifies this object as a galaxy. It is projected on the sky near the galaxy cluster ABELL 2312 (Maurogordato et al. 1997), but its systemic velocity indicates that it is a nearby object. In our opinion, it is unclear whether this is a galaxy or a Galactic object.
[j] This object is not associated with the M81 group and may be a background/foreground galaxy.
[k] According to NED, this object may be a planetary nebula.
[l] This object has also been classified as a X-ray source and a star.
[m] This object may have $D \simeq 7.1$ Mpc (from surface brightness fluctuations; Karachentsev et al. 2013) and be outside the CVn I cloud.
[n] This object may have $D \simeq 7.4$ Mpc (from the Tully–Fisher relation; Karachentsev et al. 2013) and be outside the CVn I cloud.

de Blok & Kraan-Korteweg 2013). NGC 1705 appears very isolated: the two nearest objects (LSBG F157−089 and MRSS 157−121650) are at a projected distance of ∼0.5 Mpc, but may be members of the Dorado group at $D \simeq 18$ Mpc (see Firth et al. 2006 and Evstigneeva et al. 2007, respectively). Three other objects (NGC 1533, IC 2038, and IC 2039) lie at ∼7° from NGC 1705, but they seem to be background galaxies at distances of ∼20 Mpc (based on the Tully–Fisher relation).

NGC 2366 has a H I disc with a broad extension to the south-east and a strong kinematic distortion to the north-west. Fig. 7 (left) shows an optical image overlaid with the H I emission at 15 arcsec resolution, integrated over a narrow velocity range near the systemic velocity (between ∼90 and ∼115 km s^{-1}). The gas to the north-west does not follow the rotation of the H I disc (see also fig. 3 of Oh et al. 2008) and may be associated with the secondary star-forming body to the south-west (NGC 2363). Fig 7 (right) shows a position–velocity (PV) diagram taken along the dashed line in Fig. 7 (left). Intriguingly, the PV diagram displays a steep velocity gradient coinciding with the spatial position and optical systemic velocity of NGC 2363 (indicated by the star). This may indicate that this velocity gradient is due to rotation in a local potential well. However, given the overall rotation of the H I disc of NGC 2366, this conclusion is uncertain. The NGC 2363/NGC 2366 system probably is an on-going minor merger.

NGC 4068 shows a broad H I extension to the south-east. This object is in the Canes Venatici I (CVn I) cloud, which is an extended, loose group inhabited by low-mass galaxies (Karachentsev et al. 2003).

NGC 4163 shows a H I tail to the west and, possibly, a second tail to the south (see also Hunter et al. 2012). NGC 4163 is in the CVn I cloud and lie close to several other Irrs (at $D_p \simeq 30$ kpc), including the starburst dwarf NGC 4214 and the 'compact' Irr NGC 4190 (UGC 7232). Intriguingly, NGC 4190 has been classified as a BCD by Karachentsev et al. (2013) and shows a disturbed H I morphology (see Swaters et al. 2002).

NGC 4214 has a H I disc with a well-defined spiral pattern. The H I disc is strongly warped (see LVF14) and slightly more extended to the north-west. NGC 4214 is in the CVn I cloud and has a small companion galaxy (DDO 113) at a projected distance of ∼8 kpc. DDO 113 likely is a gas-poor spheroidal (Kaisin & Karachentsev 2008). This object, indeed, is within the field-of-view of the VLA but no H I emission is detected within the covered velocity range.

NGC 4449 has an extremely extended H I distribution characterized by long filaments with column densities of ∼1 $M_\odot$ pc^{-2} (Hunter et al. 1998). A tidally disturbed companion galaxy is present towards the south-east, but it does not spatially coincide with any gaseous feature (Martínez-Delgado et al. 2012), thus its relation with the outer H I distribution is unclear. NGC 4449 is one of the most massive galaxies in the CVn I cloud (Karachentsev 2005).

NGC 5253 has a ∼4 kpc H I tail to the north at $V_{los} \simeq 400$ km s^{-1}. Our total H I map at 40 × 40 arcsec^2 resolution is slightly different from that of López-Sánchez et al. (2012) at 57.8 × 37.5 arcsec^2 resolution because we used a Gaussian-smoothed, robust-weighted data cube instead of a natural-weighted data cube. The former cube has a much more regular noise structure than the latter one, providing a better estimate of the 3σ column density sensitivity. NGC 5253 is in the CenA/M83 group; its projected distance from the spiral galaxy M83 is ∼150 kpc (Karachentsev 2005).

NGC 6789 has a regularly rotating H I disc with several asymmetric features in the outer parts. This galaxy is in the Local Void and its nearest massive companion (NGC 6946) is at a projected distance of ∼2.5 Mpc (Drozdovsky et al. 2001).

UGC 4483 has a regularly rotating H I disc with a small extension to the north-west. This galaxy is in the M81 group and lies between the group centre and the NGC 2403 subgroup (Karachentsev et al. 2002).

UGC 6456 has a H I disc that is slightly more extended to the south. The data are affected by Galactic emission, making the total H I map uncertain. Our results are in agreement with those of

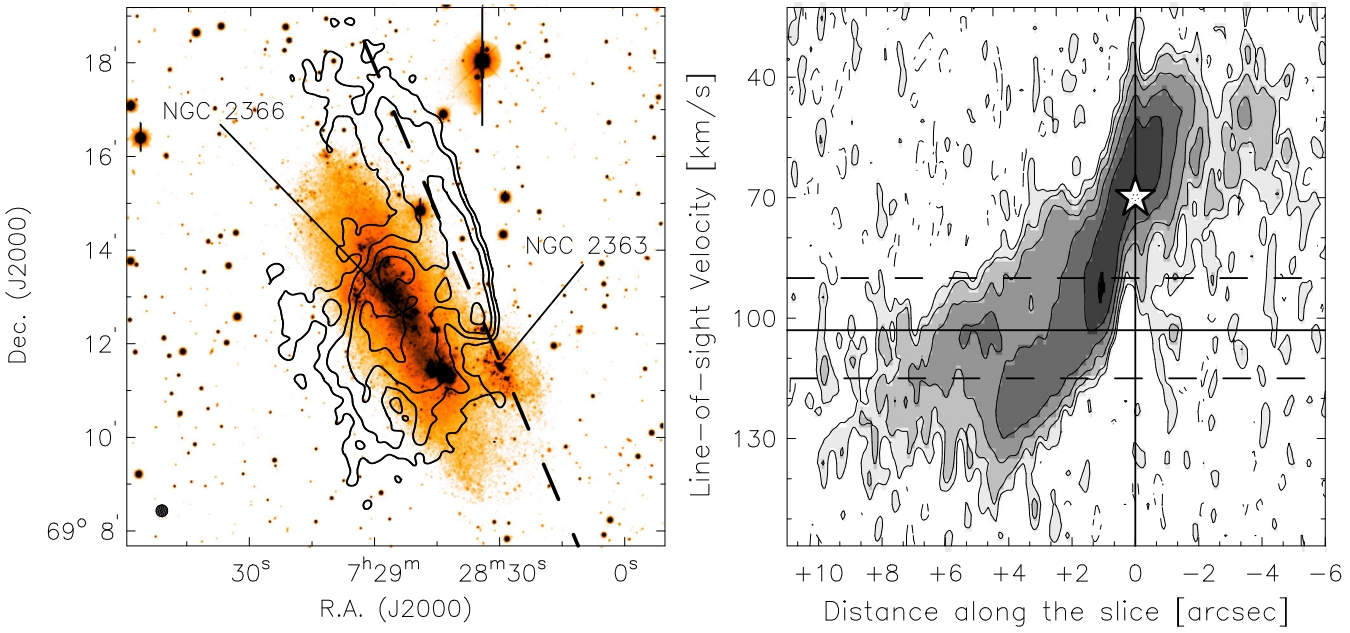

Figure 7. Kinematically anomalous gas in NGC 2363/NGC 2366. Left: *V*-band image overlaid with the H I emission at 15 arcsec resolution, integrated over a narrow velocity range near the systemic velocity of NGC 2366 (from ∼90–∼115 km s^{-1}). The H I column densities are 2, 4, 8, 16 M$_\odot$ pc^{-2}. The arrows indicate the centres of NGC 2363 and NGC 2366. The circle to the bottom-left shows the H I beam. Right: PV diagram taken along the dashed line shown in the left-hand panel. The solid, horizontal line indicates the systemic velocity of NGC 2366 (103 km s^{-1}), while the dashed, horizontal lines show the velocity range that has been used to create the H I map in the left-hand panel. The vertical line corresponds to the spatial position of NGC 2363, while the star shows its optical systemic velocity (70 km s^{-1}), as given by NED. Contours are at -1.5σ (dashed), 1.5σ, 3σ, 6σ, and 12σ, where $\sigma = 0.66$ mJy beam^{-1}.

Simpson et al. (2011). UGC 6456 lies in the periphery of the M81 group (Karachentsev 2005).

UGC 6541 has a strongly asymmetric H I distribution. Gas emission is detected only in the northern half of the galaxy. UGC 6541 is located to the north-western edge of the CVn I cloud (Karachentsev et al. 2003). Another BCD (NGC 3741; Karachentsev et al. 2013) lies at a projected distance of ∼300 kpc.

UGC 9128 has a relatively regular H I distribution, but the optical and kinematic position angles differ by ∼30°. This galaxy appears very isolated; the closest massive galaxy is the Milky Way at $D \simeq 2.2$ Mpc (Karachentsev et al. 2013).

UGCA 290 has a peculiar H I distribution that is off-set with respect to the stellar component. Our total H I map at 20 × 20 arcsec^2 resolution is less extended than the one obtained by Kovač, Oosterloo & van der Hulst (2009) using WSRT data at 52.2 × 30.9 arcsec^2 resolution, but the H I fluxes are consistent within the uncertainties, indicating that our total H I map is not missing diffuse H I emission. UGCA 290 may be part of the NGC 4631 group; its projected distance from NGC 4631 is ∼700 kpc.

I Zw 18 has been studied in detail by Lelli et al. (2012a). The total H I map presented here is slightly different from that in Lelli et al. (2012a) because it was constructed using a mask at 60 arcsec resolution (instead of 45 arcsec resolution) for consistency with the other galaxies. The most likely interpretation of this system is an interaction/merger between two (or more) gas-rich dwarfs.

I Zw 36 has an extended, asymmetric H I distribution that is kinematically connected to a central rotating disc (see Ashley, Simpson & Elmegreen 2013; LVF14). Data at 10 arcsec resolution (see Fig. 8) reveal that the H I emission forms a tail-like structure to the south at receding velocities ($V_{\rm los} \simeq$ 300–310 km s^{-1}; $V_{\rm sys} = 277$ km s^{-1}) and a broad extension to the north near the systemic velocity ($V_{\rm los} \simeq$ 270–290 km s^{-1}), possibly connected to the approaching side of the

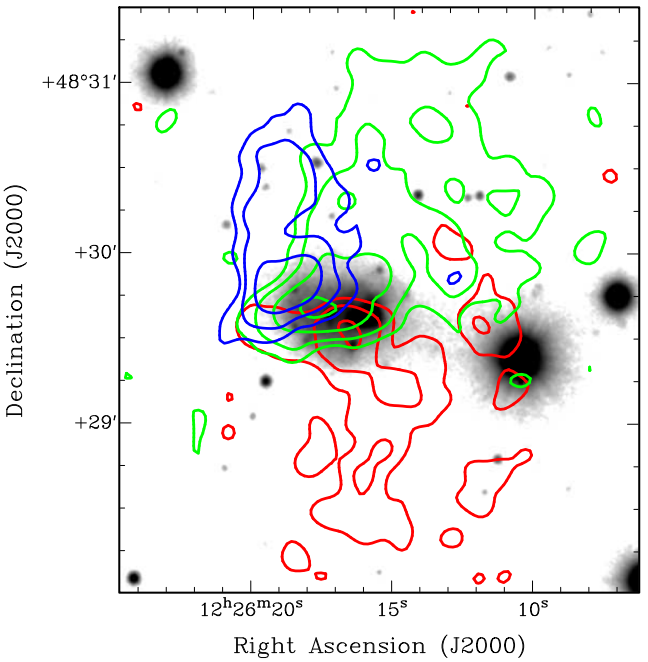

Figure 8. H I emission in I Zw 36 at 10 arcsec resolution, integrated across three velocity ranges: 250–260 km s^{-1} (blue), 275–285 km s^{-1} (green), and 300–310 km s^{-1} (red). Contours are at 1.2, 2.4, 4.8, and 9.6 M$_\odot$ pc^{-2}. Please see the electronic version of the journal for a colour version of this figure.

disc ($V_{\rm los} \simeq$ 250–260 km s^{-1}). There are no optical features associated with the extended gas down to $\mu_{\rm R} \simeq 26$ mag arcsec^{-2}. I Zw 36 is in the CVn I cloud.

SBS 1415+437 has an extended, lopsided H I disc. The galaxy is at a relatively large distance (∼13.6 Mpc), thus it is possible

that faint, nearby companions have not been identified by optical surveys.

6 DISCUSSION

In Section 3 we found that starburst dwarfs show a large variety of H I morphologies. Several of them have heavily disturbed H I morphologies, characterized by strong asymmetries, long filaments, and/or large offsets between the stellar and H I distributions. Other starburst dwarfs, instead, show minor asymmetries, characterized by H I extensions and/or small tails in the outer parts. In Section 4 we introduced the parameter A, quantifying the outer H I asymmetry, and measured it for both our sample of starburst dwarfs and a control sample of typical Irrs. We found that starburst dwarfs systematically have more asymmetric H I morphologies that typical Irrs, although there is a 'grey area' for $0.4 \lesssim A \lesssim 0.5$ where one can find both starburst and non-starburst dwarfs with lopsided H I morphologies. Lopsidedness is a common phenomenon among spirals and Irr galaxies (e.g. Baldwin, Lynden-Bell & Sancisi 1980; Verheijen & Sancisi 2001; Swaters et al. 2002), and it has been suggested that it may be due to past interactions and/or accretion events (e.g. Sancisi et al. 2008). Alternatively, one may conceive that the outer H I asymmetries are the result of gaseous outflows due to stellar feedback. This latter hypothesis seems unlikely, as we now discuss.

Hydrodynamical simulations show that gaseous outflows generally follow the path of least resistance from the interstellar medium (D'Ercole & Brighenti 1999; Mac Low & Ferrara 1999; Cooper et al. 2008) and, thus, develop perpendicularly to the galaxy major axis. Several starburst dwarfs do show diffuse Hα emission roughly perpendicular to the galaxy major axis (see e.g. fig. 7 of Lee et al. 2009), which likely traces an outflow (although the Hα gas generally does *not* escape from the galaxy potential well; e.g. Martin 1996, 1998; van Eymeren et al. 2009a,b, 2010). The H I gas in the outer regions, instead, often has a tail-like morphology and does not show any preferential direction with respect to the galaxy major axis (see Fig. 1). Moreover, in general there is little (if any) correlation between the H I and Hα emission in the outer galaxy regions; see e.g. I Zw 18 (fig. 9 of Lelli et al. 2012a) and NGC 1705 (fig. 8 of Elson et al. 2013). We also note that, if the outer H I asymmetries were due to stellar feedback, one may expect a correlation between the asymmetry parameter A and some SFR indicators, given that a higher star formation activity would produce stronger outflows and, thus, more asymmetric H I distributions. We found no convincing correlation between A and either the SFR surface density or the specific SFR (see Section 4.3). For all these reasons, we think that the H I emission in the outer regions is not due to gas outflows, but it indicates that the starburst is triggered by *external mechanisms*, such as interactions/mergers between gas-rich dwarfs or cold gas accretion from the IGM.

In Section 4.3 we found that there is a significant correlation between A and the lookback time at the peak of the star formation activity t_p (see Fig. 6, left). Galaxies hosting an 'old' burst ($\gtrsim$100 Myr) have low values of A, while galaxies hosting a 'young' burst ($\lesssim$100 Myr) have a progressively more asymmetric H I distribution. In particular, galaxies with lopsided H I morphologies ($A \lesssim 0.6$) have values of $t_p \simeq 500$ Myr that are comparable with the orbital times in the outer regions (see Fig. 6, right). This suggests that the *differential* rotation in the outer galaxy regions could have had enough time to partially regularize the H I distribution since the epoch of the interaction/accretion event that possibly triggered the starburst. In particular, galaxies with extended, strongly warped, and regularly rotating H I discs, such as NGC 4214 (LVF14) and NGC 2915 (Elson et al. 2010), may represent an advanced stage of the interaction/accretion phenomenon, as it has already been suggested by Sancisi et al. (2008). On the other hand, a galaxy like NGC 1705, which has a warped H I disc that is strongly off-set with respect to the stellar component (see LVF14), may be in an earlier stage where the outer H I gas is still in the process of settling down. This is in agreement with the very recent starburst activity ($t_p \simeq 3$ Myr) observed in this galaxy (Annibali et al. 2003).

Recent H I studies by Ekta, Chengalur & Pustilnik (2008), Ekta & Chengalur (2010), and López-Sánchez et al. (2010) have also highlighted the importance of interaction/accretion events in triggering the starburst in low-mass galaxies. In Table 6, we list further examples of starburst dwarfs with high-quality H I observations. This list is by no means complete. We have, however, carefully inspected the published total H I maps and velocity fields of these galaxies, and report their main properties in Table 6. These galaxies do *not* have accurate SFHs from *HST* observations, but are thought to be experiencing a starburst based on their blue colours, high surface brightnesses, and/or strong emission lines. We also have no direct information on the 'age' of the starburst. However, considering the observed trend between H I asymmetry and t_p, we are probably observing starburst dwarfs at different stages of the interaction/accretion process. In particular, we distinguish between four main 'classes' or 'evolutionary stages'.

(i) Starburst dwarfs that have a nearby companion ($\lesssim$200 kpc) but show *no* sign of strong interactions, such as H I bridges or tails (e.g. II Zw 33; Walter et al. 1997). These systems may either be experiencing a mild tidal interaction or represent a late stage after a fly-by.

(ii) Starburst dwarfs that are clearly interacting with a companion (e.g. II Zw 70/II Zw 71; Cox et al. 2001) or are in an advanced stage of merging (e.g. II Zw 40; van Zee et al. 1998).

(iii) Starburst dwarfs that are relatively isolated and show a heavily disturbed H I morphology (e.g. IC 10; Manthey & Oosterloo 2008), which may be due to a recent interaction/merger or cold gas accretion from the environment.

(iv) Starburst dwarfs that are relatively isolated and have an extended, lopsided H I disc (e.g. UM 439; van Zee et al. 1998) or a pronounced warp (e.g. NGC 2915; Elson et al. 2010).

Our galaxy sample includes starburst dwarfs from all these four classes. As we described in Section 5, NGC 4214 and NGC 4163 have several nearby companions belonging to the CVn I cloud and, thus, fit into class (i). Grocholski et al. (2008) argued that NGC 1569 and UGCA 290 form a pair of galaxies in the IC 432 group similar to the Large Magellanic Cloud and the Small Magellanic Cloud in the Local Group; in this case, NGC 1569 would also belong to class (i). There may be more starburst dwarf in this class, having galaxies at projected distances $D_p \lesssim$200 kpc and differences in their systemic velocities $\lesssim 300\,\mathrm{km\,s^{-1}}$, but the lack of accurate distance estimates for their potential companions prevents us from unambiguously classifying them (see Section 5). I Zw 18, NGC 4449, and NGC 2366 are probably undergoing a minor merger (see Lelli et al. 2012a, Martínez-Delgado et al. 2012, and Section 5, respectively) and, thus, belong to class (ii). I Zw 36, UGC 6431, UGCA 290, and NGC 625 can be included in class (iii), whereas UGC 4483, UGC 6456, UGC 9128, and SBS 1415+437 belong to class (iv). NGC 6789 and NGC 5253 are somewhat intermediate between class (iii) and (iv), having $A \simeq 0.6$.

The observational evidence presented so far indicates that past and on-going interaction/accretion events play an important role

Table 6. Other starburst dwarfs with high-quality H I observations.

Name(s)	Properties	References
II Zw 33 (Mrk 1039)	LSB companion II Zw 33 B	Walter et al. (1997)
HS 0822+3542	LSB companion SAO 0822+3542	Chengalur et al. (2006)
Mrk 324 (UGCA 439)	LSB companion EXG 0123−0040; H I tail?	van Zee et al. (2001)
NGC 2537 (Mrk 86)	Companion IC 2233 (Sd); outer H I arm	Matthews & Uson (2008)
UM 461/UM 462	BCD pair with lopsided H I discs	van Zee et al. (1998)
Haro 4 (Mrk 26)	Possible interaction with NGC 3510 (Sm)	Bravo-Alfaro et al. (2004)
Mrk 108 (IC 2450)	Interacting with NGC 2814 (Sb) and NGC 2820 (Sc)	Kantharia et al. (2005)
II Zw 70/ II Zw 71	Interacting pair	Cox et al. (2001)
SBS 0335−052	Interacting pair	Pustilnik et al. (2001a) and Ekta, Pustilnik & Chengalur (2009)
SBS 1129+576/577	Interacting pair	Ekta, Chengalur & Pustilnik (2006)
II Zw 40 (UGC 116)	Advanced merger	van Zee et al. (1998)
IC 10 (UGC 192)	Long H I filaments and plumes	Manthey & Oosterloo (2008)
Haro 36 (UGC 7950)	H I filament	Ashley et al. (2013)
Mrk 1418 (UGC 5151)	H I plumes and clouds	van Zee et al. (2001)
FCC 35	High-velocity H I complex	Putman et al. (1998)
Haro 2 (Mrk 33)	H I extension and small tail/cloud	Thuan, Hibbard & Lévrier (2004)
NGC 4861 (UGC 8098)	H I disc extended towards a H I cloud	Thuan et al. (2004)
Mrk 900 (NGC 7077)	Lopsided H I disc	van Zee et al. (2001)
Mrk 750	Lopsided H I disc	van Zee et al. (2001)
UM 439 (UGC 6578)	Lopsided H I disc	van Zee et al. (1998)
UM 323	Lopsided H I disc, possibly warped	van Zee et al. (2001)
UM 38	Relatively regular H I disc	van Zee et al. (2001)
NGC 2915	Extended, warped H I disc	Meurer et al. (1996) and Elson, de Blok & Kraan-Korteweg (2010)

in triggering the starburst in low-mass galaxies. Moreover, interaction/mergers between gas-rich dwarfs may provide the mechanism that forms the central concentration of mass observed in starburst dwarfs (Lelli et al. 2012a,b, 2014a). Numerical simulations, indeed, indicate that interactions/mergers between gas-rich dwarfs can lead to an overall contraction of the disc and form a central mass concentration (e.g. Bekki 2008). We stress, however, that several galaxies in our sample show remarkably symmetric optical morphologies (down to $\sim$26 mag arcsec^{-2}), whereas the H I distribution is heavily perturbed (see e.g. I Zw 36 in Fig. 8). To unambiguously identify galaxy interaction as the main triggering mechanism, one would need deep optical observations (down to $\sim$29–30 mag arcsec^{-2}) to search for stellar tidal features associated with the H I features. In the case that stellar tidal features would still remain undetected, the remaining possibility is that starburst dwarfs are directly accreting gas from the IGM. Cold flows of gas are predicted by Λ cold dark matter (ΛCDM) models of galaxy formation (Kereš et al. 2005; Dekel & Birnboim 2006). In particular, Kereš et al. (2005) argued that these cold flows might still take place at $z \simeq 0$ in low-mass galaxies residing in low-density environments. As we discussed in Section 5, most starburst dwarfs in our sample inhabit similar environments as typical Irrs, such as galaxy groups and small associations. Thus, it is unclear why cosmological cold flows would be visible only in starburst dwarfs and not in typical Irrs, unless they are highly stochastic and can rapidly trigger central bursts by bringing large amounts of gas to the bottom of the potential well. It is also unclear what the relation would be between these cold flows and the central concentration of mass (luminous and dark). Three galaxies (NGC 1705, NGC 6789, and UGC 9128), however, *seem* very isolated and show relatively regular optical morphologies down to $\mu \simeq 26\,R$ mag arcsec^{-2}. If the regular optical morphologies of these three galaxies are confirmed by deeper optical images, they may represent cases of cosmological gas accretion in the Local Universe.

7 CONCLUSIONS

We investigated the distribution and kinematics of the H I gas in the outer regions of nearby starburst dwarf galaxies, using both new and archival data. We considered 18 starburst dwarfs that have been resolved into single stars by *HST* observations, providing their recent SFHs and starburst time-scales. Our main results can be summarized as follows.

(i) Starburst dwarfs display a broad range of H I morphologies. Several galaxies show heavily disturbed H I morphologies characterized by large-scale asymmetries, long filaments, and/or strong offsets between the stellar and H I distributions, whereas other galaxies show only minor asymmetries in the outer regions.

(ii) We defined the parameter A to quantify the large-scale H I asymmetry in the outer regions and measured it for our sample of starburst dwarfs and a control sample of typical dwarf Irrs, drawn from the VLA-ANGST survey. We found that starburst dwarfs generally have higher values of A than typical Irrs, suggesting that some external mechanism triggered the starburst.

(iii) We compared the values of A with the starburst properties. We found that galaxies hosting a 'young' burst ($\lesssim$100 Myr) typically have more asymmetric H I morphologies than galaxies hosting an 'old' one ($\gtrsim$100 Myr), further indicating that there is a close link between the outer, disturbed H I distribution and the central, recent star formation. Galaxies hosting an 'old' burst likely had enough time to partially regularize their outer H I distribution, since the 'age' of the burst ($\sim$500 Myr) is comparable with the orbital time in the outer parts.

(iv) We investigated the nearby environment of the galaxies in our sample. Most of them have a potential perturber at a projected distance $\lesssim$200 kpc, thus the hypothesis of a past interaction cannot be excluded. Three galaxies (NGC 2366, NGC 4449, and I Zw 18) are probably undergoing a minor merger. Another three objects (NGC 1705, NGC 6789, and UGC 9128), instead, seem

very isolated and show regular optical morphologies down to $\mu \simeq 26\,R$ mag arcsec^{-2}, thus they *may* represent cases of cold gas accretion in the nearby Universe.

ACKNOWLEDGEMENTS

We are grateful to Renzo Sancisi for sharing his valuable insights with us. We thank Ed Elson, Deidre Hunter, and Angel R. López-Sánchez for providing us with the H I data of NGC 1705, NGC 4449, and NGC 5253, respectively. We also thanks the members of the WHISP, THINGS, LITTLE-THINGS, and VLA-ANGST projects for having made the H I data publicly available. FL acknowledges the Ubbo Emmius bursary program of the University of Groningen and the Leids Kerkhoven-Bosscha Fund. FF acknowledges financial support from PRIN MIUR 2010-2011, project 'The Chemical and Dynamical Evolution of the Milky Way and Local Group Galaxies', prot. 2010LY5N2T.

REFERENCES

Annibali F., Greggio L., Tosi M., Aloisi A., Leitherer C., 2003, AJ, 126, 2752
Annibali F. et al., 2013, AJ, 146, 144
Ashley T., Simpson C. E., Elmegreen B. G., 2013, AJ, 146, 42
Baldwin J. E., Lynden-Bell D., Sancisi R., 1980, MNRAS, 193, 313
Bekki K., 2008, MNRAS, 388, L10
Bekki K., Freeman K. C., 2002, ApJ, 574, L21
Berg D. A. et al., 2012, ApJ, 754, 98
Bouchard A., Prugniel P., Koleva M., Sharina M., 2010, A&A, 513, A54
Bravo-Alfaro H., Brinks E., Baker A. J., Walter F., Kunth D., 2004, AJ, 127, 264
Briggs D. S., 1995, BAAS, 27, 1444
Campos-Aguilar A., Moles M., 1991, A&A, 241, 358
Campos-Aguilar A., Moles M., Masegosa J., 1993, AJ, 106, 1784
Cannon J. M., McClure-Griffiths N. M., Skillman E. D., Côté S., 2004, ApJ, 607, 274
Chengalur J. N., Pustilnik S. A., Martin J., Kniazev A. Y., 2006, MNRAS, 371, 1849
Conselice C. J., 2003, ApJS, 147, 1
Cooper J. L., Bicknell G. V., Sutherland R. S., Bland-Hawthorn J., 2008, ApJ, 674, 157
Cote S., Freeman K. C., Carignan C., Quinn P. J., 1997, AJ, 114, 1313
Côté S., Carignan C., Freeman K. C., 2000, AJ, 120, 3027
Cox A. L., Sparke L. S., Watson A. M., van Moorsel G., 2001, AJ, 121, 692
Crone M. M., Schulte-Ladbeck R. E., Greggio L., Hopp U., 2002, ApJ, 567, 258
Dalcanton J. J. et al., 2009, ApJS, 183, 67
Dekel A., Birnboim Y., 2006, MNRAS, 368, 2
del Río M. S., Brinks E., Cepa J., 2004, AJ, 128, 89
D'Ercole A., Brighenti F., 1999, MNRAS, 309, 941
Drozdovsky I. O., Schulte-Ladbeck R. E., Hopp U., Crone M. M., Greggio L., 2001, ApJ, 551, L135
Ekta B., Chengalur J. N., 2010, MNRAS, 403, 295
Ekta B., Chengalur J. N., Pustilnik S. A., 2006, MNRAS, 372, 853
Ekta B., Chengalur J. N., Pustilnik S. A., 2008, MNRAS, 391, 881
Ekta B., Pustilnik S. A., Chengalur J. N., 2009, MNRAS, 397, 963
Elmegreen B. G., Zhang H.-X., Hunter D. A., 2012, ApJ, 747, 105
Elson E. C., de Blok W. J. G., Kraan-Korteweg R. C., 2010, MNRAS, 404, 2061
Elson E. C., de Blok W. J. G., Kraan-Korteweg R. C., 2011, MNRAS, 415, 323
Elson E. C., de Blok W. J. G., Kraan-Korteweg R. C., 2013, MNRAS, 429, 2550
Evstigneeva E. A., Drinkwater M. J., Jurek R., Firth P., Jones J. B., Gregg M. D., Phillipps S., 2007, MNRAS, 378, 1036
Firth P., Evstigneeva E. A., Jones J. B., Drinkwater M. J., Phillipps S., Gregg M. D., 2006, MNRAS, 372, 1856
Gallagher J. S., III, Hunter D. A., 1987, AJ, 94, 43
Gil de Paz A., Madore B. F., Pevunova O., 2003, ApJS, 147, 29
Grocholski A. J. et al., 2008, ApJ, 686, L79
Guseva N. G., Papaderos P., Izotov Y. I., Green R. F., Fricke K. J., Thuan T. X., Noeske K. G., 2003, A&A, 407, 105
Holwerda B. W., Pirzkal N., de Blok W. J. G., Bouchard A., Blyth S.-L., van der Heyden K. J., Elson E. C., 2011a, MNRAS, 416, 2401
Holwerda B. W., Pirzkal N., de Blok W. J. G., Bouchard A., Blyth S.-L., van der Heyden K. J., Elson E. C., 2011b, MNRAS, 416, 2415
Holwerda B. W., Pirzkal N., de Blok W. J. G., Blyth S.-L., 2013, MNRAS, 435, 1020
Hunter D. A., Elmegreen B. G., 2004, AJ, 128, 2170
Hunter D. A., Wilcots E. M., van Woerden H., Gallagher J. S., Kohle S., 1998, ApJ, 495, L47
Hunter D. A. et al., 2012, AJ, 144, 134
Iovino A., Melnick J., Shaver P., 1988, ApJ, 330, L17
Izotov Y. I., Thuan T. X., 1999, ApJ, 511, 639
Johnson M., Hunter D. A., Oh S.-H., Zhang H.-X., Elmegreen B., Brinks E., Tollerud E., Herrmann K., 2012, AJ, 144, 152
Kaisin S. S., Karachentsev I. D., 2008, A&A, 479, 603
Kantharia N. G., Ananthakrishnan S., Nityananda R., Hota A., 2005, A&A, 435, 483
Karachentsev I. D., 2005, AJ, 129, 178
Karachentsev I. D. et al., 2002, A&A, 383, 125
Karachentsev I. D. et al., 2003, A&A, 398, 467
Karachentsev I. D., Karachentseva V. E., Huchtmeier W. K., Makarov D. I., 2004, AJ, 127, 2031
Karachentsev I. D., Makarov D. I., Kaisina E. I., 2013, AJ, 145, 101
Kennicutt R. C., Jr, 1998, ARA&A, 36, 189
Kereš D., Katz N., Weinberg D. H., Davé R., 2005, MNRAS, 363, 2
Kobulnicky H. A., Skillman E. D., 1997, ApJ, 489, 636
Kovač K., Oosterloo T. A., van der Hulst J. M., 2009, MNRAS, 400, 743
Lauberts A., Valentijn E. A., 1989, The Surface Photometry Catalogue of the ESO-Uppsala Galaxies. European Southern Observatory, Garching
Lee J. C., Salzer J. J., Law D. A., Rosenberg J. L., 2000, ApJ, 536, 606
Lee J. C. et al., 2009, ApJ, 706, 599
Lelli F., Verheijen M., Fraternali F., Sancisi R., 2012a, A&A, 537, A72
Lelli F., Verheijen M., Fraternali F., Sancisi R., 2012b, A&A, 544, A145
Lelli F., Fraternali F., Verheijen M., 2014a, A&A, 563, A27
Lelli F., Verheijen M., Fraternali F., 2014b, A&A, 566, A71 (LVF14)
López-Sánchez Á. R., 2010, A&A, 521, A63
López-Sánchez A. R., Koribalski B., van Eymeren J., Esteban C., Popping A., Hibbard J., 2010, in Verdes-Montenegro L., Del Olmo A., Sulentic J., eds, ASP Conf. Ser. Vol. 421, Galaxies in Isolation: Exploring Nature Versus Nurture. Astron. Soc. Pac., San Francisco, p. 65
López-Sánchez Á. R., Koribalski B. S., van Eymeren J., Esteban C., Kirby E., Jerjen H., Lonsdale N., 2012, MNRAS, 419, 1051
Lotz J. M., Primack J., Madau P., 2004, AJ, 128, 163
Mac Low M., Ferrara A., 1999, ApJ, 513, 142
McQuinn K. B. W. et al., 2010, ApJ, 721, 297
McQuinn K. B. W., Skillman E. D., Dalcanton J. J., Cannon J. M., Dolphin A. E., Holtzman J., Weisz D. R., Williams B. F., 2012, ApJ, 759, 77
Manthey E., Oosterloo T., 2008, in Minchin R., Momjian E., eds, AIP Conf. Proc. Vol. 1035, The Evolution of Galaxies Through the Neutral Hydrogen Window. Am. Inst. Phys., New York, p. 156
Marlowe A. T., Meurer G. R., Heckman T. M., 1999, ApJ, 522, 183
Martin C. L., 1996, ApJ, 465, 680
Martin C. L., 1998, ApJ, 506, 222
Martínez-Delgado D. et al., 2012, ApJ, 748, L24
Mateo M. L., 1998, ARA&A, 36, 435
Matthews L. D., Uson J. M., 2008, AJ, 135, 291
Maurogordato S., Proust D., Cappi A., Slezak E., Martin J. M., 1997, A&AS, 123, 411
Méndez D. I., Esteban C., 2000, A&A, 359, 493
Méndez D. I., Esteban C., Balcells M., 1999, AJ, 117, 1229

Meurer G. R., Carignan C., Beaulieu S. F., Freeman K. C., 1996, AJ, 111, 1551
Meurer G. R., Staveley-Smith L., Killeen N. E. B., 1998, MNRAS, 300, 705
Noeske K. G., Iglesias-Páramo J., Vílchez J. M., Papaderos P., Fricke K. J., 2001, A&A, 371, 806
Noguchi M., 1988, A&A, 201, 37
Noordermeer E., van der Hulst J. M., Sancisi R., Swaters R. A., van Albada T. S., 2005, A&A, 442, 137
Oh S., de Blok W. J. G., Walter F., Brinks E., Kennicutt R. C., 2008, AJ, 136, 2761
Ott J. et al., 2012, AJ, 144, 123
Papaderos P., Izotov Y. I., Thuan T. X., Noeske K. G., Fricke K. J., Guseva N. G., Green R. F., 2002, A&A, 393, 461
Pustilnik S., Ugryumov A. V., Lipovetsky V. A., Thuan T. X., Guseva N., 1995, ApJ, 443, 499
Pustilnik S. A., Brinks E., Thuan T. X., Lipovetsky V. A., Izotov Y. I., 2001a, AJ, 121, 1413
Pustilnik S. A., Kniazev A. Y., Lipovetsky V. A., Ugryumov A. V., 2001b, A&A, 373, 24
Putman M. E., Bureau M., Mould J. R., Staveley-Smith L., Freeman K. C., 1998, AJ, 115, 2345
Salzer J. J., 1989, ApJ, 347, 152
Sancisi R., Fraternali F., Oosterloo T., van der Hulst T., 2008, A&AR, 15, 189
Schulte-Ladbeck R. E., Hopp U., Greggio L., Crone M. M., 2000, AJ, 120, 1713
Schulte-Ladbeck R. E., Hopp U., Greggio L., Crone M. M., Drozdovsky I. O., 2001, AJ, 121, 3007
Silk J., Wyse R. F. G., Shields G. A., 1987, ApJ, 322, L59
Simpson C. E. et al., 2011, AJ, 142, 82
Skillman E. D., Côté S., Miller B. W., 2003, AJ, 125, 593
Stil J. M., Israel F. P., 1998, A&A, 337, 64
Stil J. M., Israel F. P., 2002, A&A, 392, 473
Swaters R. A., Balcells M., 2002, A&A, 390, 863
Swaters R. A., van Albada T. S., van der Hulst J. M., Sancisi R., 2002, A&A, 390, 829
Taylor C., Brinks E., Skillman E. D., 1993, AJ, 105, 128
Taylor C. L., Brinks E., Grashuis R. M., Skillman E. D., 1995, ApJS, 99, 427
Taylor C. L., Thomas D. L., Brinks E., Skillman E. D., 1996, ApJS, 107, 143
Telles E., Maddox S., 2000, MNRAS, 311, 307
Telles E., Terlevich R., 1995, MNRAS, 275, 1
Terlevich R., Melnick J., Masegosa J., Moles M., Copetti M. V. F., 1991, A&AS, 91, 285
Thilker D. A. et al., 2010, ApJ, 714, L171
Thuan T. X., Izotov Y. I., 2005, ApJS, 161, 240
Thuan T. X., Hibbard J. E., Lévrier F., 2004, AJ, 128, 617
Trentham N., Tully R. B., Verheijen M. A. W., 2001, MNRAS, 325, 385
van Eymeren J., Marcelin M., Koribalski B., Dettmar R.-J., Bomans D. J., Gach J.-L., Balard P., 2009a, A&A, 493, 511
van Eymeren J., Marcelin M., Koribalski B. S., Dettmar R.-J., Bomans D. J., Gach J.-L., Balard P., 2009b, A&A, 505, 105
van Eymeren J., Koribalski B. S., López-Sánchez Á. R., Dettmar R.-J., Bomans D. J., 2010, MNRAS, 407, 113
van Zee L., Skillman E. D., Salzer J. J., 1998, AJ, 116, 1186
van Zee L., Salzer J. J., Skillman E. D., 2001, AJ, 122, 121
Verheijen M., Sancisi R., 2001, A&A, 370, 765
Walter F., Brinks E., Duric N., Klein U., 1997, AJ, 113, 2031
Walter F., Brinks E., de Blok W. J. G., Bigiel F., Kennicutt R. C., Jr, Thornley M. D., Leroy A., 2008, AJ, 136, 2563
Weisz D. R. et al., 2011, ApJ, 739, 5

APPENDIX A: ESTIMATING THE NOISE IN A TOTAL H I MAP

In their appendix A, Verheijen & Sancisi (2001) describe how to calculate the noise in a total H I map obtained using a mask on an hanning-tapered data cube, in which all the channel maps are kept during the analysis. Here we derive similar formulas that can be used to construct signal-to-noise ratio maps in two different cases: (i) a uniform-tapered data cube, as it is the case for the WHISP data and our new WRST and VLA observations; and (ii) an online hanning-tapered data cube, in which half of the channel maps are discarded during the observations, as it is the case for the THINGS/LITTLE-THINGS data and other archival VLA observations.

A1 Uniform taper

If the observations are made using a uniform velocity taper, the noise $\sigma^{\rm u}$ in two channel maps will be independent. When N uniform-tapered channel maps are added at the spatial position (x, y), the noise $\sigma^{\rm u}_N$ in the total H I map will increase by a factor $\sqrt{N}$, thus $\sigma^{\rm u}_N(x, y) = \sqrt{N(x, y)}\sigma^{\rm u}$. However, before the channel maps are added to form a total H I map, the continuum emission is subtracted, introducing further noise in the channel maps. Here we assume that the continuum map $C^{\rm u}$ is constructed by averaging N_1 and N_2 line-free channel maps at the high- and low-velocity ends of the data cube, respectively. Thus, one has

$$C^{\rm u} = \frac{1}{2}\left(\frac{1}{N_1}\sum_{j=1}^{N_1} U_j + \frac{1}{N_2}\sum_{j=1}^{N_2} U_j\right), \tag{A1}$$

and the noise $\sigma^{\rm u}_C$ in the continuum map is given by

$$\sigma^{\rm u}_C = \frac{1}{2}\sqrt{\frac{1}{N_1} + \frac{1}{N_2}}\sigma^{\rm u}. \tag{A2}$$

If U_i is the value of a pixel in the ith uniform-tapered channel map, the line emission $L^{\rm u}_i$ is given by $L^{\rm u}_i = U_i - C^{\rm u}$ and the noise $\sigma^{\rm lu}_i$ in $L^{\rm u}_i$ is given by

$$\sigma^{\rm lu}_i = \sqrt{1 + \frac{1}{4}\left(\frac{1}{N_1} + \frac{1}{N_2}\right)}\sigma^{\rm u}. \tag{A3}$$

When N uniform-tapered and continuum-subtracted channel maps are added, the signal $L^{\rm u}_N$ at a position (x, y) of the total H I map is given by

$$L^{\rm u}_N(x, y) = \sum_{j=1}^{N(x,y)} L^{\rm u}_j = \sum_{j=1}^{N(x,y)} U_j - N(x, y)C, \tag{A4}$$

and the noise $\sigma^{\rm lu}_N$ is given by

$$\begin{aligned}\sigma^{\rm lu}_N(x, y) &= \sqrt{N(x, y)\sigma^{\rm u^2} + N(x, y)^2\sigma^{\rm u^2}_C} \\ &= \sqrt{1 + \frac{N(x, y)}{4}\left(\frac{1}{N_1} + \frac{1}{N_2}\right)}\sqrt{N(x, y)}\sigma^{\rm u}.\end{aligned} \tag{A5}$$

A2 Online hanning taper

If the observations are made using an hanning taper, the data cube is smoothed in velocity and the noise in two adjacent channel maps is no longer independent. When the online hanning smoothing option of the VLA is used, half of the channel maps are discarded. If U_i and

Table A1. Adding N online hanning-tapered channel maps.

Channel	U_{i-1}	U_i	U_{i+1}	U_{i+2}	U_{i+3}	...	U_{i+2N-3}	U_{i+2N-2}	U_{i+2N-1}
i	1/4	1/2	1/4						
$i+2$			1/4	1/2	1/4				
...					...	...	...		
$i+2N-2$							1/4	1/2	1/4
	1/4	1/2	1/2	1/2	1/2	...	1/2	1/2	1/4

O_i are, respectively, the values of a pixel in the ith uniform-tapered and online hanning-tapered channel maps, one has

$$O_i = \frac{1}{4}U_{i-1} + \frac{1}{2}U_i + \frac{1}{4}U_{i+1},$$
$$O_{i+1} = \frac{1}{4}U_i + \frac{1}{2}U_{i+1} + \frac{1}{4}U_{i+2},$$
$$O_{i+2} = \frac{1}{4}U_{i+1} + \frac{1}{2}U_{i+2} + \frac{1}{4}U_{i+3}, \quad \text{(A6)}$$

and the i+1th channel map is discarded during the observations. The remaining channel maps ith and i+2th are *not* independent, because both contain a quarter of the emission U_{i+1}. Thus, when N online hanning-smoothed channel maps are added, the noise $\sigma_N^{\rm o}$ does not increase by a factor $\sqrt{N}$, but by a factor $\sqrt{N-\frac{3}{4}}\frac{4}{\sqrt{2}\sqrt{6}}$, as we show in the following. The noise $\sigma^{\rm o}$ in the online hanning smoothed channel maps is equal to $\frac{\sqrt{6}}{4}\sigma^{\rm u}$ (see Verheijen & Sancisi 2001). The total signal O_N is given by

$$O_N = O_i + O_{i+2} + O_{i+4} + O_{i+6} + \cdots + O_{i+2(N-1)}. \quad \text{(A7)}$$

As illustrated in Table A1, one has

$$O_N = \frac{1}{4}U_{i-1} + \frac{1}{2}U_i + \frac{1}{2}U_{i+1} + \cdots + \frac{1}{2}U_{i+2N-2} + \frac{1}{4}U_{i+2N-1}, \quad \text{(A8)}$$

and the noise $\sigma_N^{\rm o}$ is given by

$$\sigma_N^{\rm o} = \sqrt{\left(\frac{1}{4}\right)^2 + \left(\frac{1}{2}\right)^2 (2N-2) + \left(\frac{1}{4}\right)^2}\,\sigma^{\rm u}$$
$$= \frac{1}{\sqrt{2}}\sqrt{N-\frac{3}{4}}\sigma^{\rm u} = \sqrt{N-\frac{3}{4}}\frac{4}{\sqrt{2}\sqrt{6}}\sigma^{\rm o}. \quad \text{(A9)}$$

The continuum map $C^{\rm o}$ is now constructed by averaging N_1 and N_2 line-free channel maps at the high- and low-velocity ends of the online hanning-tapered data cube, thus the noise $\sigma_C^{\rm o}$ in $C^{\rm o}$ is given by

$$\sigma_C^{\rm o} = \frac{1}{2\sqrt{2}}\sqrt{\frac{1}{N_1^2}\left(N_1 - \frac{3}{4}\right) + \frac{1}{N_1^2}\left(N_2 - \frac{3}{4}\right)}\,\sigma^{\rm u} \quad \text{(A10)}$$
$$\equiv \frac{1}{\sqrt{2}}A\sigma^{\rm u} = \frac{4}{\sqrt{2}\sqrt{6}}A\sigma^{\rm o}. \quad \text{(A10)}$$

The line-emission in the ith channel map is given by $L_i^{\rm o} = O_i - C^{\rm o}$, thus the noise in $L_i^{\rm o}$ is given by

$$\sigma_i^{\rm lo} = \sqrt{1 + \frac{4}{3}A^2}\sigma^{\rm o}. \quad \text{(A11)}$$

When N online hanning-tapered and continuum-subtracted channel maps are added, the signal $L_N^{\rm o}$ at a position (x, y) of the total H I maps is given by

$$L_N^{\rm o}(x,y) = \frac{1}{4}U_{i-1} + \frac{1}{2}U_i + \cdots + \frac{1}{2}U_{i+2N-2} + \frac{1}{4}U_{i+2N-1} - N(x,y)C^{\rm o}, \quad \text{(A12)}$$

and the noise $\sigma_N^{\rm lo}$ at (x, y) is given by

$$\sigma_N^{\rm lo}(x,y) = \sqrt{N(x,y) - \frac{3}{4} + N^2(x,y)A^2}\,\frac{4}{\sqrt{2}\sqrt{6}}\sigma^{\rm o}. \quad \text{(A13)}$$

Note that this equation differs by a factor $1/\sqrt{2}$ from the one given by Verheijen & Sancisi (2001), which is valid in the case that all the hanning-tapered channel maps are kept during the data analysis.

This paper has been typeset from a TEX/LATEX file prepared by the author.